



**HAL**  
open science

## Experimental Safety Analysis of R-Min, an Underactuated Parallel Robot

Guillaume Jeanneau, Vincent Begoc, Sébastien Briot

► **To cite this version:**

Guillaume Jeanneau, Vincent Begoc, Sébastien Briot. Experimental Safety Analysis of R-Min, an Underactuated Parallel Robot. *Journal of Mechanisms and Robotics*, 2023, 15 (3), pp.031004-1 – 031004-15. 10.1115/1.4056765 . hal-03942318

**HAL Id: hal-03942318**

**<https://hal.science/hal-03942318>**

Submitted on 23 Jan 2023

**HAL** is a multi-disciplinary open access archive for the deposit and dissemination of scientific research documents, whether they are published or not. The documents may come from teaching and research institutions in France or abroad, or from public or private research centers.

L'archive ouverte pluridisciplinaire **HAL**, est destinée au dépôt et à la diffusion de documents scientifiques de niveau recherche, publiés ou non, émanant des établissements d'enseignement et de recherche français ou étrangers, des laboratoires publics ou privés.

# Experimental Safety Analysis of R-Min, an underactuated parallel Robot

Guillaume Jeanneau<sup>a,b,d</sup>

Vincent Bégoc<sup>a,c,\*</sup>

Sébastien Briot<sup>a,d</sup>

<sup>a</sup> Laboratoire des Sciences du Numérique de Nantes (LS2N)

UMR CNRS 6004, 44321 Nantes, France

<sup>b</sup> École Centrale de Nantes (ECN)

<sup>c</sup> Institut Catholique d'Arts et Métiers (ICAM)

<sup>d</sup> Centre National de la Recherche Scientifique (CNRS)

Emails: {Guillaume.Jeanneau,Sebastien.Briot}@ls2n.fr, Vincent.Begoc@icam.fr

The R-Min robot is an intrinsically safe parallel manipulator dedicated to pick-and-place operations. The proposed architecture is based on a five-bar mechanism, with additional passive joints in order to obtain a planar seven-bar mechanism with two degrees of underactuation, allowing the robot to reconfigure in case of a collision. A preload bar is added between the base and the end-effector to constrain the additional degrees of freedom. This article presents an analysis of the workspace and of the safety performances of the R-Min robot, and it compares them with those of the five-bar mechanism, in order to evaluate the benefits of introducing underactuation in a parallel architecture to obtain intrinsically safer robots. The geometrico-static model of the R-Min robot is formulated as an optimisation problem. The direct and inverse kinemato-static models are derived from the geometrico-static model and they allow to express the singularity conditions of the R-Min robot. An analysis of the singularity loci is carried out among the robot's workspace. A controller based on the dynamic model is proposed and experimentally validated on a prototype of the R-Min robot. Finally, the safety performances of the R-Min robot are evaluated experimentally and they are compared with that of an equivalent five-bar mechanism, using the maximum impact force as a safety criteria in accordance with recent international standards.

---

\* Address all correspondence to this author.

## 1 INTRODUCTION

### 1.1 Context and state of the art

The introduction, in the industry, of collaborative robotic cells able to safely share their workspace with humans requires finding solutions to reduce the risk to an acceptable level. Improving the safety of robots can be achieved by sensing or control strategies (reviews can be found in [1, 2]). However, those strategies are limited by the bandwidth and the response time of the controller, making it hardly suitable to face with the highly dynamics and unpredictable nature of human displacements. Therefore, strategies based on the mechanical design to obtain intrinsically safe robots are worth being deeply investigated.

A first strategy consists in reducing the mass of the robot links in order to reduce the reflected mass at the impact [3, 4, 5] and thus to mitigate the impact severity. However, when applied to a serial architecture, this strategy is limited by the rigidity of the resulting architecture and the accuracy of the end-effector's position. Another strategy consists in using intrinsically compliant actuators such as SEA [6] (Series Elastic Actuators), VSA [7] (Variable Stiffness Actuators) or the DM<sup>2</sup> (Distributed Macro-Mini) actuation approach [8]. This principle allows to decouple the inertia of the links from that of the motor, thus reducing the reflected mass at the impact. If the use of SEA leads to concepts suffering from poor accuracy, the VSA and DM<sup>2</sup> lead to complex and costly actuators. Therefore, other interesting concepts have been proposed based on the use of preloaded compliant mechanisms [9, 10, 11, 12, 13] or clutch mechanisms [14]. Such

solutions have been used in multi-link serial architectures, however the experimental evaluation of their safety are often conducted on a single link mechanism.

The use of a parallel architecture to design safe robots has been little investigated in the literature [15], although it allows to reduce the mass of the moving links. In previous works [16], we introduced the R-Min robot, an underactuated parallel robot, whose design is based on the architecture of the five-bar mechanism in which two supplementary passive joints are added. The obtained robot can self-configure in case of a collision with the environment allowing to mitigate the severity of an impact with a human being. However, no experimental proof of the safety performances of this concept has been provided so far.

Assessing the safety of a collaborative robotic application requires the use of safety-related criteria. The automotive industry widely used the HIC [17] (Head Injury Criteria) to evaluate the severity of a crash accident for human beings. However, it appears that this index is not well suited to analyze the severity of an impact with a robot [18, 19], since the velocity of the robot tip is much lower than that of a car. More recently, bio-mechanical thresholds have been furnished in the standard ISO/TS 15066 [20] for 29 different body parts, based on the experimental analysis of the pain tolerance of 100 healthy subjects [21], following the early works of [22]. These thresholds define the maximum quasi-static (resp. transient) force and pressure which can be continuously (resp. temporary) applied by the robot on a human body part.

Multiple experimental works investigated the evaluation of the safety performances of new concepts of safe robot. Early works were carried out by the DLR institute in a crash-test centre dedicated to car certification. They used a dummy sitting in a car seat, and mounted a force sensor at the end of the DLR LWR III robot [18]. Such an experimental setup is obviously complex and costly to reproduce. Recently, the consortium of the European project COVR, dedicated to safety-related issues, published protocols to help end-users and system integrators to measure the force and pressure during a constrained [23] or unconstrained impact [24] (an impact is said to be constrained when the impacted human body region is clamped between the robot and the wall or any other rigid and fixed part of the workspace). This protocol involves the use of appropriate force and pressure sensors but also a dedicated mechanical system which imitates the bio-mechanical properties of the human body, including a spring to mimic the stiffness of the impacted human body part and a foam to mimic the non-linear properties of the skin. The characteristics of the spring (stiffness)

and the foam (thickness and hardness) are specified in a former study [25] of the DGUV (Deutsche Gesetzliche Unfallversicherung) institute.

## 1.2 Contribution highlights

The aim of this paper is to demonstrate the interest of introducing underactuation and compliance in the mechanical architecture of a parallel robot in order to improve the safety of the robot. The performances of the R-Min robot are thus compared with those of the five-bar mechanism from which it is inspired. First, the workspace of the R-Min robot is compared with that of the five-bar mechanism. Therefore, the direct and inverse geometrico-static model and kinemato-static model of the R-Min robot are introduced in a forward and unified manner. The geometrico-static model is formulated as an optimization problem minimizing the potential energy of the robot, and it conducts, through a numerical analysis, to the definition of the robot's workspace. Singularity conditions are derived from the kinemato-static model allowing to determine the singularity loci in the robot's workspace. Then, the safety performances of the R-Min robot are experimentally compared with those of the five-bar mechanism. Therefore, a prototype of the R-Min robot was designed and manufactured. This prototype can be turned into a five-bar mechanism with equivalent inertia properties allowing a fair comparison. Following recent international standards, a measurement device is used to measure the maximum impact force and evaluate the severity of an impact. A set of experiments is defined in order to analyze the effect of multiple parameters on safety such as the robot's configuration at the time of impact, the position of the contact on the robot, the velocity of the robot, the stiffness of the preload bar.

The paper is constructed as follows: Section 2 presents the R-Min robot and the manufactured prototype. In Section 3, the geometrico-static and kinemato-static models of the R-Min robot are introduced and a singularity analysis is presented. The Cartesian workspace of the R-Min robot is drawn and compared with that of the five-bar mechanism. The effect of the robot's stiffness on the size of the workspace is analyzed. In Section 4, the dynamic model of the robot is presented as well as the associated computed torque controller. The tracking performances of the controller are then evaluated experimentally, on a prototype of the R-Min robot. Section 5 presents the experimental setup and the experimental protocol designed to allow the comparison of the safety performances of the R-Min robot with respect to that of the five-bar mechanism based on the measurement of the impact force. The effect of the stiffness of the preload bar on

safety is analyzed. Conclusions are drawn in Section 6.

## 2 PRESENTATION OF THE R-MIN ROBOT

In this Section, the kinematic architecture of the robot is introduced. Its behavior when faced with different operating scenarios (in particular during a collision with an operator) is illustrated. The corresponding prototype is introduced for further numerical and experimental analysis.

### 2.1 Description of the R-Min kinematic architecture

The R-Min robot is an underactuated parallel mechanism designed as a proof of concept for pick-and-place operations in a collaborative cell. Its architecture presented on Fig. 1a is inspired from the five-bar parallel mechanism depicted on Fig. 1b. The traditional five-bar parallel mechanism is composed of two parallel legs made with four links in totality, which are linked through three passive revolute joints at points  $O_{12}$ ,  $O_{22}$  and  $P$  and actuated by two motors located on revolute joints at points  $O_{i1}$  ( $i = \{1, 2\}$  the index of the leg). The resulting five-bar mechanism has two dofs (degrees of freedom) and is thus fully actuated and able to position its end-effector with a high rigidity.

Even if such a parallel architecture allows to reduce the moving masses in comparison with a serial architecture, a five-bar mechanism may still be harmful in case of a collision with a human because of its high stiffness. Therefore, the R-Min robot was designed so as to keep the interesting inertia properties of the five-bar mechanism while adding underactuation in the architecture in order to bring reconfiguration possibilities in case of impact. The resulting design, deeper described below, is composed of an underactuated seven-bar mechanism and a preload system to constrain the robot's configuration in the normal operating mode (Fig. 1a).

The seven-bar parallel mechanism is actuated by two motors located on revolute joints at points  $O_{i1}$ , and composed of passive revolute joints at points  $O_{i2}$ ,  $O_{i3}$  and  $P$  ( $i = \{1, 2\}$ ). All joint axes are aligned along the  $y$ -axis normal to the plane  $\mathcal{P}_0 : (A, \mathbf{x}, \mathbf{z})$ . This mechanism has four dofs (two more than the five-bar mechanism) making it underactuated with two unconstrained dofs. At this stage, the resulting chain  $O_{12}O_{13}PO_{23}O_{22}$  would have no rigidity making such robot of little practicability. We therefore introduce a preload system whose kinematic chain is composed of two passive revolute joints at points  $A$  and  $P$  (axes aligned along the  $y$  axis), a passive prismatic joint aligned along  $\overrightarrow{AP}$  (thus lying in  $\mathcal{P}_0$ ) and a compression spring exerting a force between points

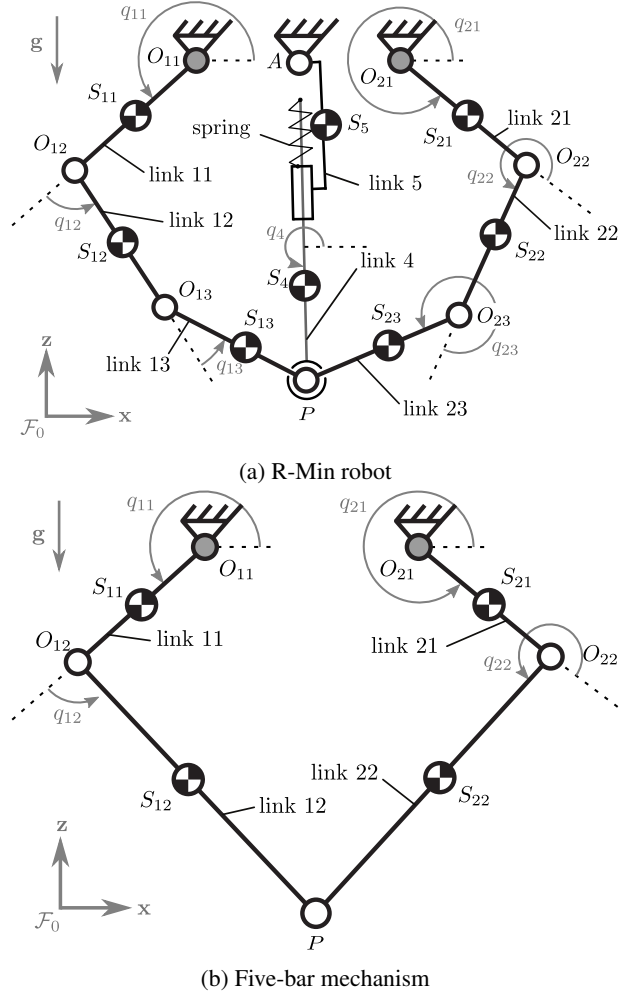


Fig. 1: Kinematic chains of (a) the R-Min robot and (b) the five-bar mechanism.

$A$  and  $P$ . This preload system plays the same role as elastic elements introduced in the design of underactuated hands [26], i.e. it drives the unconstrained dofs of the robot and kinematically constrains its configuration. This permits to tense the two distal legs  $O_{12}O_{13}P$  and  $O_{22}O_{23}P$  in order to obtain a robot stiff enough to be controlled, but less stiff than a traditional five-bar mechanism for safety purpose. In addition, since the preload system is located between the two legs, it cannot collide with an operator. This practical solution avoids adding masses on external legs (such as installing a torsion spring on passive joints  $O_{i3}$  of the seven-bar mechanism), providing a safer design.

In Figure 2, the configuration of the R-Min robot is illustrated in two different situations: during a pick-and-place trajectory, when no contact occurs (Fig. 2a) and

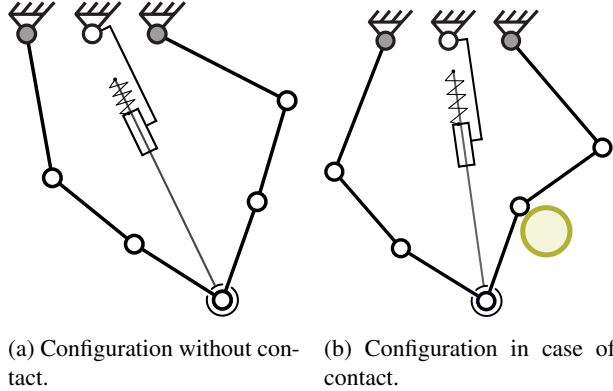


Fig. 2: Representation of the configuration of the R-Min robot during a pick-and-place trajectory: (a) without contact, the R-Min robot lies in a configuration close to the five-bar mechanism due to the force exerted by the preload bar so that the end-effector is precisely positioned, (b) when a collision occurs on the distal link, the robot self-configures to mitigate the impact force.

when a collision occurs on distal links (Fig. 2b). When the robot is subject to gravity effect only (including a payload at the end-effector), points  $O_{i2}$ ,  $O_{i3}$  and  $P$  are close to be aligned thanks to the preload system (Fig. 2a). As a result, the configuration of the R-Min robot is close to that of the five-bar mechanism and the position of the end-effector can be precisely determined, making this solution practicable for pick-and-place operations. On the other hand, when loadings likely to appear during an impact with a human are applied on the robot (on a distal link), it encounters large internal reconfigurations (Fig. 2b). This behavior should avoid transmitting a large part of the robot’s kinetic energy during impact, since a large part of the collision energy will be dissipated through the reconfiguration of the robot. This behaviour makes the R-Min robot a good candidate for safe physical interactions during pick-and-place operations, as it will be confirmed experimentally in what follows.

## 2.2 Presentation of the R-Min prototype

A prototype of the R-Min robot was manufactured based on the kinematic architecture previously defined, and is presented in Fig. 3. The key features of the design of this prototype are described below:

- All links are made in aluminium hollow tubes of circular cross-section, with (a) an external diameter of 30 mm, a thickness of 5 mm for proximal links 11 and 21 (Fig. 1a), and (b) an external diameter of 20 mm, a thickness of 2 mm for all other links.

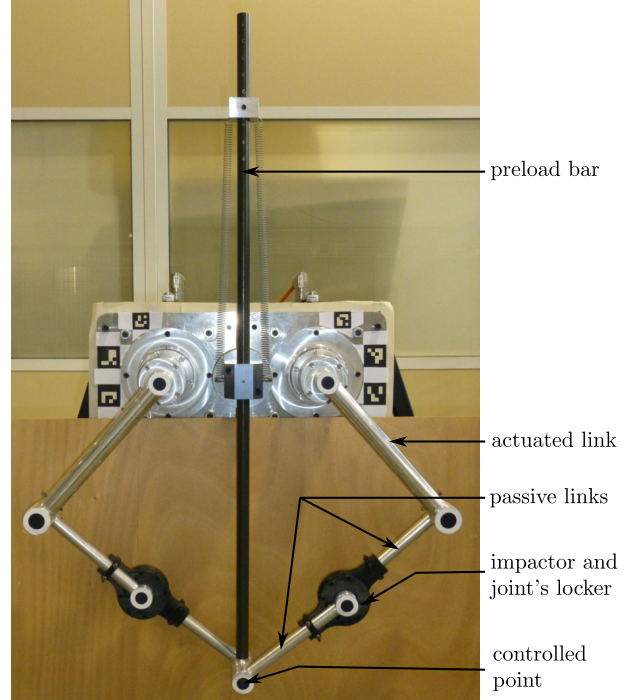


Fig. 3: Prototype of the R-Min robot. This prototype can be turned into an equivalent five-bar mechanism by removing the preload system and locking the two passive joints located at point  $O_{i3}$  ( $i = \{1, 2\}$ ).

- Passive joints are made with bronze plain bearings instead of ball bearings, to lighten the mechanism.
- The compression spring of the preload system is replaced by a set of two traction springs in order to avoid the self-locking effect of the translational guidance.
- Two direct drive motors SIMOTICS S-1FL6 are used (maximum torque of 23.9 Nm when using motor torque control).

The geometric and inertia properties of the R-Min robot are provided in Table 1. Two interchangeable springs of the preload system are indicated. In the following, the robot with the default spring ( $k_t = 111.2$  N/m) is referred to as R-Min, while the robot with the stiffer spring ( $k_t = 239.2$  N/m) is referred to as R-Min<sup>+</sup>.

The R-Min prototype can be turned into a five-bar mechanism, by removing the preload system and locking the two passive joints located at  $O_{i3}$ . This solution allows to obtain two robots with comparable dimensions, inertia and contact geometry, and thus to obtain a fair comparison of the robots performances. The geometric and inertia properties of the obtained five-bar mechanism are

Table 1: Geometric, inertia properties and design parameters of the prototype of the R-Min robot.

Link	Length	Mass	Inertia <sup>a</sup>	COM <sup>b</sup>
$(i; j)$	$\ell_{i,j}$ (m)	$m_{i,j}$ (kg)	$J_{i,j}$ (kg.m <sup>2</sup> )	$x_{i,j}$ (m)
(1&2;1)	0.28	6.92	0.0348	0.0148
(1&2;2)	0.2	0.302	0.007	0.126
(1&2;3)	0.2	0.250	0.0037	0.086
(-;4)	0.87	0.54	0.173	-0.429
(-;5)	-	0.81	0.004	0
$\ell_{O_{11}O_{21}} = 0.25$ m				
Parameters of the preload bar spring: Default setting: $k_t = 111.2$ N/m, $\ell_0 = 82.7$ mm R-Min <sup>+</sup> setting: $k_t = 239.2$ N/m, $\ell_0 = 102.5$ mm				

<sup>a</sup>Moments of inertia around  $\mathbf{y}$  are provided at the COM.

<sup>b</sup>Center of masses  $S_{ij}$  (Fig. 1a) are located on the lines  $O_{ij}O_{ij+1}$ .  $x_{i,j}$  is the distance from  $S_{ij}$  to  $O_{ij}$ .

Table 2: Geometric, inertia properties and design parameters of the prototype of the equivalent five-bar mechanism.

Link	Length	Mass	Inertia	COM
$(i; j)$	$\ell_{i,j}$ (m)	$m_{i,j}$ (kg)	$J_{i,j}$ (kg.m <sup>2</sup> )	$x_{i,j}$ (m)
(1&2;1)	0.28	6.92	0.0348	0.0148
(1&2;2)	0.40	0.59	0.0348	0.213
$\ell_{O_{11}O_{21}} = 0.25$ m				

provided in Tab. 2.

### 3 WORKSPACE ANALYSIS OF THE R-MIN ROBOT

In this section, the computation of the geometrico-static model of the R-Min robot is presented (in a more unified way than in [27]). The kinemato-static model<sup>1</sup> is derived from the geometrico-static model and allows to express the singularity conditions. The workspace of the R-Min robot is computed numerically and compared with

<sup>1</sup>Following [28], we prefer to replace the word kinetostatic by the word kinemato-static. Indeed, the former is an assembly of the words kinetics and statics, and is not related with our present interest in kinematics, i.e. with the study of the motion.

that of the five-bar mechanism.

### 3.1 Geometrico- and kinemato-static models of R-Min robot

#### 3.1.1 Geometrico-static problem

The R-Min robot being underactuated, its equilibrium configuration is obtained at a minimum of the potential energy  $U$ . The robot configuration is parameterized with the joint angles  $q_{ij}$  (with  $i = \{1, 2\}$  the index of the leg and  $j = \{1, 2, 3\}$  the index of the link) defining the angle between the links  $(i, j)$ ,  $q_4$ , the direction of the preload system and  $\rho$  its length. In what follows, we will denote as  $\mathbf{q}_a = [q_{11} \ q_{21}]^T \in \mathbb{R}^2$  the vector of the active joint coordinates,  $\mathbf{q}_d = [q_{12} \ q_{13} \ q_{22} \ q_{23}]^T \in \mathbb{R}^4$  the vector of the passive joint coordinates (excluding the preload system) and  $\mathbf{p} = [x \ z]^T \in \mathbb{R}^2$  the end-effector position vector expressed in the frame  $\mathcal{F}_0$ .

In order to solve the geometrico-static problem, for a given value of the motor angles  $\mathbf{q}_a$  (considered to be blocked), it is necessary to find the configuration  $\mathbf{q}_{dp} = [\mathbf{q}_d^T \ \mathbf{p}^T]^T \in \mathbb{R}^6$  which minimizes the robot potential energy (33), under geometric constraints (1). Indeed, due to the closed-chain nature of the robot, the variables  $\mathbf{q}_a$ ,  $\mathbf{q}_d$  and  $\mathbf{p}$  are not independent. Four constraint equations grouped in the vector  $\boldsymbol{\phi} = [\boldsymbol{\phi}_1^T \ \boldsymbol{\phi}_2^T]^T$  can be defined:

$$\boldsymbol{\phi}_i = \mathbf{0} = \overrightarrow{OO_{i1}} + \ell_{i1}\mathbf{u}_{i1} + \ell_{i2}\mathbf{u}_{i2} + \ell_{i3}\mathbf{u}_{i3} - \mathbf{p} \quad (1)$$

with  $i = \{1, 2\}$  the index of the leg and  $\mathbf{u}_{ij} = \left[ \cos \left( \sum_{k=1}^j q_{ik} \right) \ \sin \left( \sum_{k=1}^j q_{ik} \right) \right]^T$  the direction vector of the link  $(i, j)$ .

Mathematically speaking, the geometrico-static problem can be formulated as:

$$\begin{aligned} \mathbf{q}_{dp} &= \operatorname{argmin} U(\mathbf{q}_a, \mathbf{q}_d, \mathbf{p}) \\ &\text{subject to } \boldsymbol{\phi}(\mathbf{q}_a, \mathbf{q}_d, \mathbf{p}) = \mathbf{0} \end{aligned} \quad (2)$$

The total potential energy of the robot  $U$  can be expressed as a function of the coordinates  $\mathbf{q}_a$ ,  $\mathbf{q}_d$  and  $\mathbf{p}$ . For the sake of conciseness, details of the computation are given in Appendix A. This optimization problem can be reformulated using the augmented Lagrangian function defined as:

$$\mathcal{L} = U(\mathbf{q}_a, \mathbf{q}_d, \mathbf{p}) + \boldsymbol{\phi}^T(\mathbf{q}_a, \mathbf{q}_d, \mathbf{p})\boldsymbol{\lambda} \quad (3)$$

where  $\boldsymbol{\lambda} \in \mathbb{R}^4$  is a vector of Lagrange multipliers. Solutions to (2) can be found by solving the first-order stability conditions [29]  $\nabla_{\mathbf{q}_{dp}, \boldsymbol{\lambda}} \mathcal{L} = \mathbf{0}$ , which are formulated

as follows:

$$\begin{cases} \mathbf{h}(\mathbf{q}_a, \mathbf{q}_d, \mathbf{p}, \boldsymbol{\lambda}) = \mathbf{0} \\ \boldsymbol{\phi}(\mathbf{q}_a, \mathbf{q}_d, \mathbf{p}) = \mathbf{0} \end{cases} \quad (4)$$

with  $\mathbf{h}(\mathbf{q}_a, \mathbf{q}_d, \mathbf{p}, \boldsymbol{\lambda}) = \nabla_{\mathbf{q}_{dp}} U + \nabla_{\mathbf{q}_{dp}} \boldsymbol{\phi} \boldsymbol{\lambda}$ , the gradient of the Lagrangian with respect to  $\mathbf{q}_{dp}$ .

The system of equations (4) is composed of 10 equations, and contains 12 unknowns  $(\mathbf{q}_a, \mathbf{q}_d, \mathbf{p}, \boldsymbol{\lambda})$ . Therefore, it can be solved by fixing two of the unknowns to a desired value, in order to get either the forward geometrico-static model (FGSM) or the inverse geometrico-static model (IGSM). Since the solutions to Eq. (4) cannot be obtained analytically, a numerical solver for nonlinear systems of equations must be used. In this work, we used the Matlab implementation of the Levenberg-Marquardt algorithm implemented in the *fsolve* function.

**Forward geometrico-static model** By fixing the value of  $\mathbf{q}_a$  to a given value  $\mathbf{q}_a^*$ , it is possible to compute a solution  $(\mathbf{q}_d^*, \mathbf{p}^*, \boldsymbol{\lambda}^*) \in \mathbb{R}^{10}$  to Eq. (4).

**Inverse geometrico-static model** In the same manner, by fixing the value of  $\mathbf{p}$  to a given value  $\mathbf{p}^*$ , a solution  $(\mathbf{q}_a^*, \mathbf{q}_d^*, \boldsymbol{\lambda}^*) \in \mathbb{R}^{10}$  to Eq. (4) can be found.

**Second-order stability condition** The computed configuration  $(\mathbf{q}_a^*, \mathbf{q}_d^*, \mathbf{p}^*, \boldsymbol{\lambda}^*)$  is not necessarily a stable configuration, since it is not necessarily a minimizer of the potential energy  $U$ , but could be a maximizer or a saddle point. In order to assess the stability of a configuration satisfying the first-order condition given in Eq. (4), second-order conditions must be checked as detailed in [29]. These conditions can be formulated using the following two matrices:

- The Hessian matrix of the Lagrangian function with respect to  $\mathbf{q}_{dp}$ :

$$\begin{aligned} \mathbf{H}(\mathbf{q}_a^*, \mathbf{q}_d^*, \mathbf{p}^*, \boldsymbol{\lambda}^*) &= \nabla_{\mathbf{q}_{dp} \mathbf{q}_{dp}}^2 \mathcal{L}(\mathbf{q}_a^*, \mathbf{q}_d^*, \mathbf{p}^*, \boldsymbol{\lambda}^*) \\ &= \mathbf{D}_{\mathbf{q}_{dp}} \mathbf{h}(\mathbf{q}_a^*, \mathbf{q}_d^*, \mathbf{p}^*, \boldsymbol{\lambda}^*) \end{aligned} \quad (5)$$

- A matrix  $\mathbf{Z} \in \mathbb{R}^{6 \times 2}$  spanning the null space of the transposed gradient of the constraints:

$$\mathbf{Z} \in \text{Ker} \left( \nabla_{\mathbf{q}_{dp}} \boldsymbol{\phi}^T(\mathbf{q}_a^*, \mathbf{q}_d^*, \mathbf{p}^*, \boldsymbol{\lambda}^*) \right) \quad (6)$$

Then, the configuration  $(\mathbf{q}_a^*, \mathbf{q}_d^*, \mathbf{p}^*, \boldsymbol{\lambda}^*)$  is stable if the projected (or reduced) Hessian  $\mathbf{H}_z = \mathbf{Z}^T \mathbf{H} \mathbf{Z}$  is positive definite, i.e. if  $\mathbf{H}_z \succ 0$  [29].

### 3.1.2 Kinemato-static modelling of the R-Min robot

The kinemato-static model of the robot can be obtained by differentiating the geometrico-static model (4) with respect to time:

$$\begin{cases} \mathbf{D}_{\mathbf{q}_a} \mathbf{h} \dot{\mathbf{q}}_a + \mathbf{D}_{\mathbf{p}} \mathbf{h} \dot{\mathbf{p}} + \mathbf{D}_{\mathbf{q}_d} \mathbf{h} \dot{\mathbf{q}}_d + \mathbf{D}_{\boldsymbol{\lambda}} \mathbf{h} \dot{\boldsymbol{\lambda}} = \mathbf{0} \\ \mathbf{D}_{\mathbf{q}_a} \boldsymbol{\phi} \dot{\mathbf{q}}_a + \mathbf{D}_{\mathbf{p}} \boldsymbol{\phi} \dot{\mathbf{p}} + \mathbf{D}_{\mathbf{q}_d} \boldsymbol{\phi} \dot{\mathbf{q}}_d = \mathbf{0} \end{cases} \quad (7)$$

Equation (7) can be simplified by left-multiplying its first line by matrix  $\mathbf{Z}^T$  defined in (6), noticing that  $\mathbf{D}_{\boldsymbol{\lambda}} \mathbf{h} = \nabla_{\mathbf{q}_{dp}} \boldsymbol{\phi}$ . We then obtain:

$$\mathbf{A} \dot{\mathbf{q}}_a + \mathbf{P} \dot{\mathbf{p}} + \mathbf{D} \dot{\mathbf{q}}_d = \mathbf{0} \quad (8)$$

with  $\mathbf{A} = \begin{bmatrix} \mathbf{Z}^T \mathbf{D}_{\mathbf{q}_a} \mathbf{h} \\ \mathbf{D}_{\mathbf{q}_a} \boldsymbol{\phi} \end{bmatrix} \in \mathbb{R}^{6 \times 2}$ ,  $\mathbf{P} = \begin{bmatrix} \mathbf{Z}^T \mathbf{D}_{\mathbf{p}} \mathbf{h} \\ \mathbf{D}_{\mathbf{p}} \boldsymbol{\phi} \end{bmatrix} \in \mathbb{R}^{6 \times 2}$  and  $\mathbf{D} = \begin{bmatrix} \mathbf{Z}^T \mathbf{D}_{\mathbf{q}_d} \mathbf{h} \\ \mathbf{D}_{\mathbf{q}_d} \boldsymbol{\phi} \end{bmatrix} \in \mathbb{R}^{6 \times 4}$

The system of equations (8) is made of 6 equations, and contains 8 unknowns  $(\dot{\mathbf{q}}_a, \dot{\mathbf{q}}_d, \dot{\mathbf{p}})$ . Therefore, by fixing two of the unknowns to a desired value, Eq. (8) can be solved, in order to get either the forward kinemato-static model (FKSM) or the inverse kinemato-static model (IKSM).

**Forward kinemato-static model** It allows to express the end-effector velocity  $\dot{\mathbf{p}}$  and the passive joint velocities  $\dot{\mathbf{q}}_d$  as a function of the motor velocities  $\dot{\mathbf{q}}_a$ :

$$\begin{bmatrix} \dot{\mathbf{p}} \\ \dot{\mathbf{q}}_d \end{bmatrix} = -\mathbf{G}_{\mathbf{PD}}^{-1} \mathbf{A} \dot{\mathbf{q}}_a \quad (9)$$

where  $\mathbf{G}_{\mathbf{PD}} = [\mathbf{P} \ \mathbf{D}] \in \mathbb{R}^{6 \times 6}$ . The conditions of degeneracy of the matrix  $\mathbf{G}_{\mathbf{PD}}$  are discussed later.

**Inverse kinemato-static model** It allows to express the motor velocities  $\dot{\mathbf{q}}_a$  and the passive joint velocities  $\dot{\mathbf{q}}_d$  as a function of the end-effector velocity  $\dot{\mathbf{p}}$ :

$$\begin{bmatrix} \dot{\mathbf{q}}_a \\ \dot{\mathbf{q}}_d \end{bmatrix} = -\mathbf{G}_{\mathbf{AD}}^{-1} \mathbf{P} \dot{\mathbf{p}} \quad (10)$$

where  $\mathbf{G}_{\mathbf{AD}} = [\mathbf{A} \ \mathbf{D}] \in \mathbb{R}^{6 \times 6}$ . The conditions of degeneracy of the matrix  $\mathbf{G}_{\mathbf{AD}}$  are discussed in the next paragraph.

**Singularity analysis** The system of equations (8) is analogous to that of a continuum parallel robot [30], as detailed in [31]. Based on this paper, several types of singularities may appear for this system of equations, among which the main ones are:

- Type 1 singularities: appear when matrix  $\mathbf{G}_{AD}$  is rank deficient, while the matrices  $\mathbf{A}$  and  $\mathbf{D}$  are full rank. These are singularities of the IKSM: In them, a motion of the motors do not lead to a motion of the end-effector in some given direction. They define the workspace boundaries.
- Type 2 singularities: appear when matrix  $\mathbf{G}_{PD}$  is rank deficient, while the matrices  $\mathbf{P}$  and  $\mathbf{D}$  are full rank. These are singularities of the FKSM: For a fixed position of the motors, a small displacement of the end-effector is allowed. As shown in [31], they define the boundaries of the stable configuration domains and lead to a loss of stiffness of the robot.
- Type 3 singularities: appear when matrices  $\mathbf{G}_{AD}$  and  $\mathbf{G}_{PD}$  are rank deficient at the same time, while the matrices  $\mathbf{A}$ ,  $\mathbf{P}$  and  $\mathbf{D}$  are all full rank. These are a combination of both other types of singularities.

Other types of singularity may be found, as mentioned in [31], but do not appear in the study of the prototype of the R-Min robot, therefore we do not recall them.

### 3.2 Robot workspace analysis

In what follows, the algorithm provided in [27] is used to draw the Cartesian workspace of the R-Min robot. Since, there exist multiple solutions to the geometrico-static problem of the R-Min robot (as detailed in [27]), the following inequalities are added in order to keep only the set of solutions corresponding to the configuration of the robot depicted in Fig. 2a:

$$-4\pi/3 < q_{11} < -\pi/6 \quad (11)$$

$$-5\pi/6 < q_{21} < \pi/3 \quad (12)$$

$$y < 0 \quad (13)$$

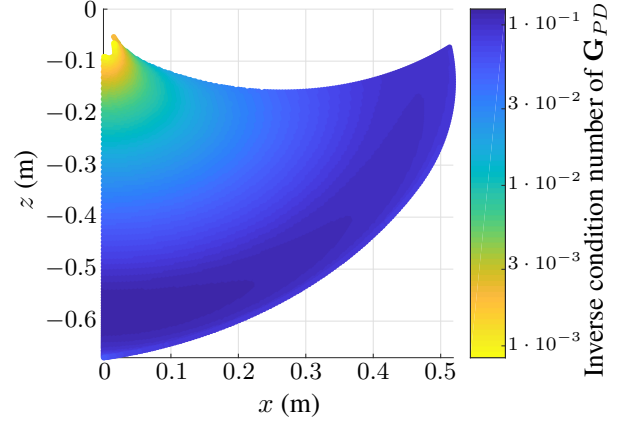
$$-\pi/2 < q_{i3} < \pi/2 \quad (14)$$

$$0 < \theta_1 < \pi \quad (15)$$

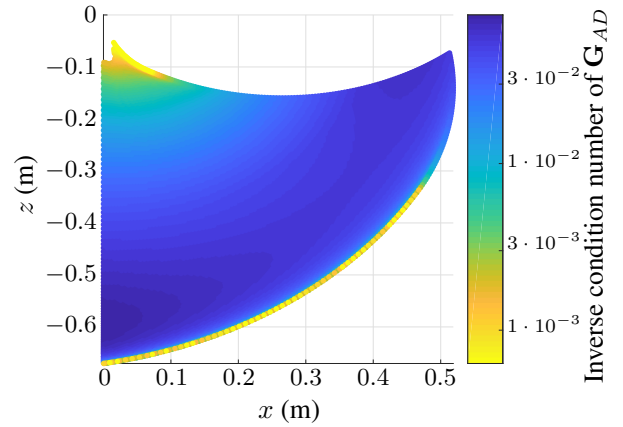
$$-\pi < \theta_2 < 0 \quad (16)$$

with  $\theta_i$  being the angle between  $\overrightarrow{O_{i1}O_{i2}}$  and  $\overrightarrow{O_{i2}O_P}$ . The search of the workspace is performed only in half of the joint space since the robot is symmetric, therefore the additional constraint  $\pi - q_{21} < q_{11}$  is considered.

The working mode depicted in Fig. 2a is suitable for multiple reasons:



(a) Inverse condition number of matrix  $\mathbf{G}_{PD}$  projected in the workspace



(b) Inverse condition number of matrix  $\mathbf{G}_{AD}$  in the workspace

Fig. 4: Inverse condition numbers of matrices (a)  $\mathbf{G}_{PD}$  and (b)  $\mathbf{G}_{AD}$  plotted in the Cartesian workspace of the R-Min robot.

- both distal arms can fold in case of a collision with a human,
- the preload bar does not present any risk of injury since it lies between both distal arms,
- it offers a large Cartesian space for the controlled point,
- the weight of the payload has no (or little) effect on the position of the end-effector, as shown in [27].

The obtained workspace for the current prototype is represented on Fig. 4. It corresponds to the set of *stable* solutions to the geometrico-static problem, satisfying inequalities (11)-(16). The parameters of the prototype provided in Tab. 1 have been considered for the computation with the default setting of the preload system.

The values of the inverse condition numbers of the



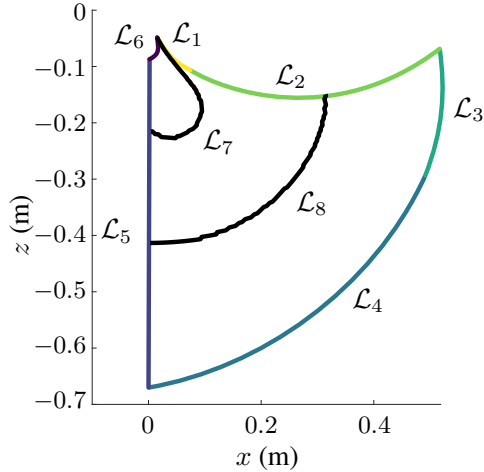


Fig. 5: Decomposition of the workspace boundaries of the R-Min robot.

matrices  $\mathbf{G}_{PD}$  and  $\mathbf{G}_{AD}$  are respectively plotted on Fig. 4a and Fig. 4b allowing to localize the singularity loci<sup>2</sup> in the Cartesian workspace. Several observations can be made:

- Type 2 singularity loci are only present in the top of the workspace, thus allowing to have a large region without issues in terms of stability,
- The boundaries of the workspace are made of either (a) singularities or (b) the joint limits given in Eqs. (11) to (14).

Figure. 5 decomposes the boundaries of the workspace of the R-Min robot: curves  $\mathcal{L}_1$ ,  $\mathcal{L}_4$  and  $\mathcal{L}_6$  correspond to singularities (as it can be seen on Fig. 4), while  $\mathcal{L}_2$  and  $\mathcal{L}_3$  correspond to the mechanical limits of both motors (resp.  $q_{21} < \pi/3$  and  $q_{11} < -\pi/6$ ),  $\mathcal{L}_5$  corresponds to the symmetry of the robot. When considering unlimited motor torques,  $\mathcal{L}_1$  to  $\mathcal{L}_6$  thus represent the boundaries of the workspace for the R-Min robot. When considering the motor torque limitations of our prototype (23.9 Nm), a new boundary appears which depends on the stiffness of the preload system. This boundary can significantly reduce the workspace. Thus, the curve  $\mathcal{L}_7$  (resp.  $\mathcal{L}_8$ ) indicates the position for which one motor reaches the maximal value 23.9 Nm for the R-Min robot (resp. for R-Min<sup>+</sup>).

The whole workspace of the R-Min robot is drawn

<sup>2</sup>In the present work, we compute the condition number of matrices whose components have non-homogeneous units. This is valid as long as we intend to analyze the degeneracy of the corresponding matrices, and not to characterize the physical performance of the robot [32], which is not the case in this paper.

on Fig. 6a. When no limitation of the motor torque is considered, the workspace of the R-Min robot is close to that of the five-bar mechanism corresponding to Tab. 2 (Fig. 6b). However, when considering the maximal torque that can be delivered by each motor (23.9 Nm for the prototype), the size of the workspace of the R-Min robot decreases. This workspace is represented for two interchangeable springs in the preload system, with a stiffness  $k_t = 111.2$  N/m and a free length  $\ell_0 = 82.7$  mm for the R-Min robot (Fig.6c) and  $k_t = 239.2$  N/m,  $\ell_0 = 102.5$  mm for the R-Min<sup>+</sup> robot (Fig.6d). Indeed, when increasing the spring stiffness, the size of the workspace decreases because motors cannot deliver enough torque to compensate the wrench applied by the preload system at the end-effector.

We may thus conclude that the spring stiffness of the preload system has a considerable impact on the size of the robot workspace: the lower the stiffness, the larger the workspace. In addition, a lower stiffness would intuitively be related to a safer robot as will be discussed later in section 5. However, since the R-Min robot is underactuated, there exist internal oscillations of the passive joints during a trajectory, whose amplitude is related to the robot stiffness. These oscillations are directly related to the positioning accuracy of the end-effector which is evaluated in the following section.

## 4 DYNAMIC MODELING AND CONTROL OF THE R-MIN ROBOT

In this section, the dynamic model of the R-Min robot is introduced. Based on this model, a modified version of a computed torque controller is proposed. The tracking performances of the implemented controller are then evaluated experimentally.

### 4.1 Dynamic model of the R-Min robot

The dynamic model of the R-Min robot is derived from the Lagrange equations. Since the robot has four dofs, it can be parameterized by four independent coordinates that will be denoted by the vector  $\mathbf{q}_g$ , defined as  $\mathbf{q}_g = [\mathbf{q}_a^T \ \mathbf{q}_u^T]^T \in \mathbb{R}^4$ , with  $\mathbf{q}_a = [q_{11} \ q_{21}]^T$  and  $\mathbf{q}_u = [q_{12} \ q_{22}]^T$ . The remaining coordinates defining the configuration of the robot are grouped into the vector  $\mathbf{q}_c = [q_{13} \ q_{23} \ \mathbf{p}^T]^T \in \mathbb{R}^4$ . The dynamic model is thus given by:

$$\begin{bmatrix} \boldsymbol{\tau} \\ \mathbf{0} \\ \mathbf{0} \end{bmatrix} + \begin{bmatrix} \nabla_{\mathbf{q}_a} \phi \\ \nabla_{\mathbf{q}_u} \phi \\ \nabla_{\mathbf{q}_c} \phi \end{bmatrix} \boldsymbol{\nu} = \begin{bmatrix} \boldsymbol{\tau}_{\mathbf{q}_a} \\ \boldsymbol{\tau}_{\mathbf{q}_u} \\ \boldsymbol{\tau}_{\mathbf{q}_c} \end{bmatrix} \quad (17)$$

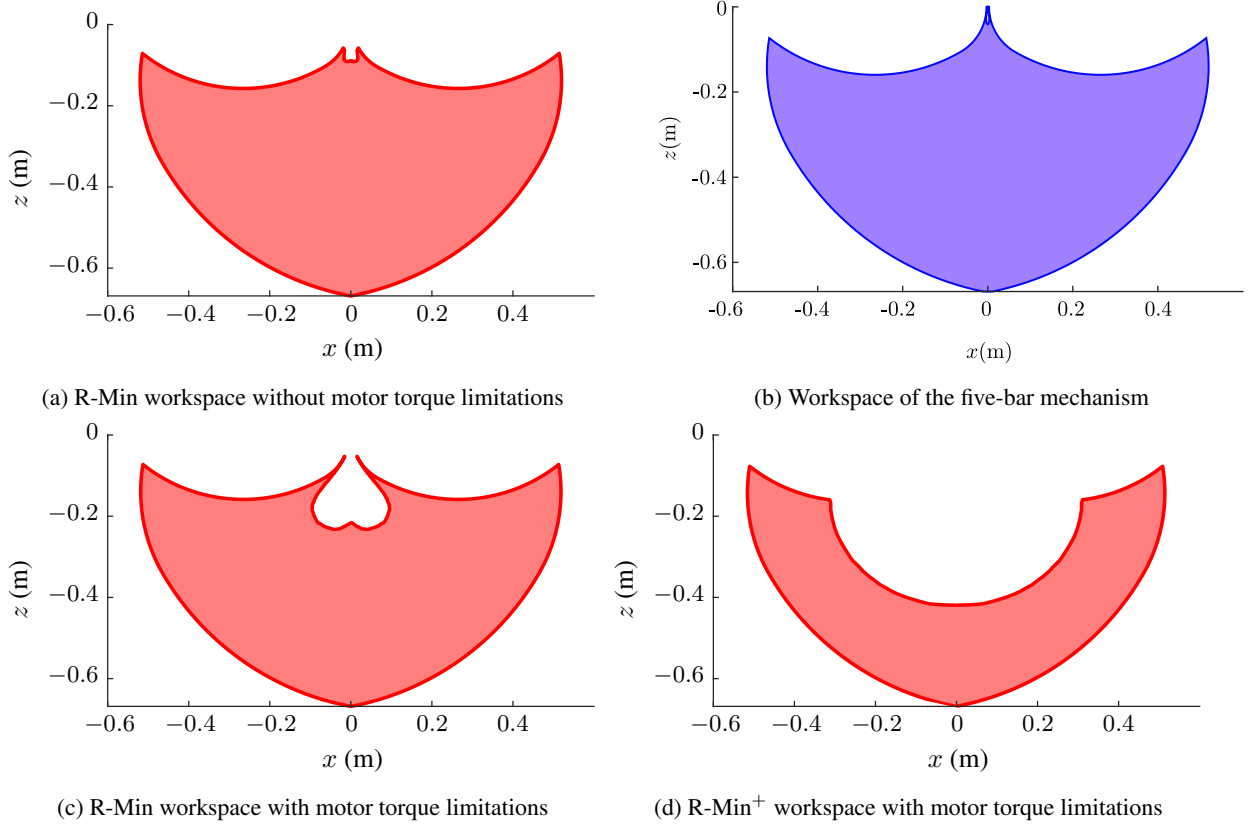


Fig. 6: (a-b) Representation of the Cartesian workspace of the R-Min robot for two different values of the spring stiffness in the preload bar considering a maximum motor torque of 23.9 Nm, compared with (c) the Cartesian workspace of the five-bar mechanism. The robot parameters given Tab. 1 have been considered.

with  $\tau_{\mathbf{q}_a}$ ,  $\tau_{\mathbf{q}_u}$  and  $\tau_{\mathbf{q}_c}$ , the generalised torques associated to the coordinates  $\mathbf{q}_a$ ,  $\mathbf{q}_u$  and  $\mathbf{q}_c$ , obtained using the equations of Lagrange  $\tau_{\mathbf{q}_k} = \frac{d}{dt} \left( \frac{\partial L}{\partial \dot{\mathbf{q}}_k} \right)^T - \left( \frac{\partial L}{\partial \mathbf{q}_k} \right)^T$  with  $k = \{a, u, c\}$ .  $L = E - U$  is the robot Lagrangian. For the sake of conciseness, the expressions of the potential energy  $U$  and the kinetic energy  $E$  are detailed in appendices A and B.  $\boldsymbol{\tau} \in \mathbb{R}^2$  is the vector of the motor input efforts and  $\boldsymbol{\nu} \in \mathbb{R}^4$  is a vector of Lagrange multipliers (which should not be confused with vector  $\boldsymbol{\lambda}$  introduced in the augmented Lagrangian formulation of the optimization problem in Section 3.1.1).

This model can also be rewritten under the form below, by removing the Lagrange multipliers  $\boldsymbol{\nu}$ , using the third line of eq. (17):

$$\begin{bmatrix} \boldsymbol{\tau} \\ \mathbf{0} \end{bmatrix} = \begin{bmatrix} \tau_{\mathbf{q}_a} \\ \tau_{\mathbf{q}_u} \end{bmatrix} - \begin{bmatrix} \nabla_{\mathbf{q}_a} \boldsymbol{\phi} \\ \nabla_{\mathbf{q}_u} \boldsymbol{\phi} \end{bmatrix} (\nabla_{\mathbf{q}_c} \boldsymbol{\phi})^{-1} \tau_{\mathbf{q}_c} \quad (18)$$

where  $\nabla_{\mathbf{q}_c} \boldsymbol{\phi} \in \mathbb{R}^{4 \times 4}$  is a square and invertible matrix.

Finally, after some tedious undetailed mathematical simplifications, and by replacing the expressions of the variables in the vector  $\mathbf{q}_c$  and their time-derivatives by their expressions as a function of  $\mathbf{q}_g$ ,  $\dot{\mathbf{q}}_g$ ,  $\ddot{\mathbf{q}}_g$ , the dynamic model can be obtained under the following standard form [33]:

$$\begin{bmatrix} \boldsymbol{\tau} \\ \mathbf{0} \end{bmatrix} = \begin{bmatrix} \mathbf{M}_{11}(\mathbf{q}_g) & \mathbf{M}_{12}(\mathbf{q}_g) \\ \mathbf{M}_{21}(\mathbf{q}_g) & \mathbf{M}_{22}(\mathbf{q}_g) \end{bmatrix} \begin{bmatrix} \ddot{\mathbf{q}}_a \\ \ddot{\mathbf{q}}_u \end{bmatrix} + \begin{bmatrix} \mathbf{c}_1(\mathbf{q}_g, \dot{\mathbf{q}}_g) \\ \mathbf{c}_2(\mathbf{q}_g, \dot{\mathbf{q}}_g) \end{bmatrix} \quad (19)$$

where  $\mathbf{M}_{kl} \in \mathbb{R}^{2 \times 2}$  ( $k, l = \{1, 2\}$ ) are submatrices composing the robot inertia matrix, and  $\mathbf{c}_k \in \mathbb{R}^2$  are vectors containing the centrifugal, Coriolis, gravity and spring effects. It should be noted that friction terms in the joints could also be added in the vectors  $\mathbf{c}_k$  by using the methodology presented in [34].

## 4.2 Robot controller

A modified version of the Computed Torque Controller [33] is applied for the control of the R-Min robot. For computing the motor torques, let us modify the equations of the dynamic model as follows. First, using the bottom of Eq. (19), we get:

$$\ddot{\mathbf{q}}_u = -\mathbf{M}_{22}^{-1}\mathbf{M}_{21}\ddot{\mathbf{q}}_a - \mathbf{M}_{22}^{-1}\mathbf{c}_2 \quad (20)$$

Then, introducing this expression of  $\ddot{\mathbf{q}}_u$  in the top of Eq. (19), the input torques  $\boldsymbol{\tau}$  can be obtained as follows:

$$\boldsymbol{\tau} = (\mathbf{M}_{11} - \mathbf{M}_{12}\mathbf{M}_{22}^{-1}\mathbf{M}_{21}) \ddot{\mathbf{q}}_a + \mathbf{c}_1 - \mathbf{M}_{12}\mathbf{M}_{22}^{-1}\mathbf{c}_2 \quad (21)$$

In Equation (21), the terms  $\mathbf{M}_{kl}$  and  $\mathbf{c}_k$  depend obviously of  $\mathbf{q}_a$ ,  $\dot{\mathbf{q}}_a$  and their time derivatives. However, the R-Min prototype (presented in section 2) is equipped with only two sensors positioned on both motors, which is not enough to compute the full robot configuration. It was then necessary either to predict the behaviour of the robot or to make an assumption on the robot's configuration. In order to simplify the problem, and because the preload system tense the distal arms, angles  $q_{13}$ ,  $q_{23}$  and their time derivatives are assumed to be null at any time, allowing to estimate  $\mathbf{q}_u$  and its time derivatives based on the second line of Eq. (7). This hypothesis is of course not true in practice, but this approximation will be compensated when controlling the input efforts  $\boldsymbol{\tau}$  thanks to the use of an integral term, as proposed in the following equation, derived from (21):

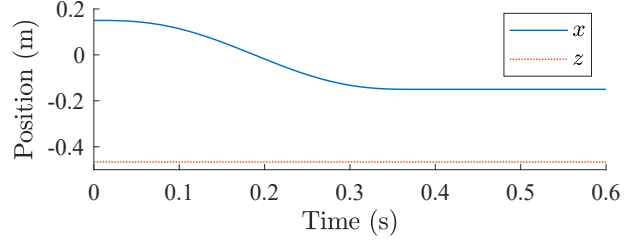
$$\begin{aligned} \boldsymbol{\tau} = & (\mathbf{M}_{11} - \mathbf{M}_{12}\mathbf{M}_{22}^{-1}\mathbf{M}_{21}) \left( \ddot{\mathbf{q}}_a^* \right. \\ & + k_i \int (\mathbf{q}_a^* - \mathbf{q}_a) + k_p (\mathbf{q}_a^* - \mathbf{q}_a) \\ & \left. + k_d (\dot{\mathbf{q}}_a^* - \dot{\mathbf{q}}_a) \right) + \mathbf{c}_1 - \mathbf{M}_{12}\mathbf{M}_{22}^{-1}\mathbf{c}_2 \end{aligned} \quad (22)$$

with  $\mathbf{q}_a^*$ ,  $\dot{\mathbf{q}}_a^*$  and  $\ddot{\mathbf{q}}_a^*$ , the desired position, velocity and acceleration, respectively, and  $k_d$ ,  $k_p$ ,  $k_i$  three gains defined by [33]:

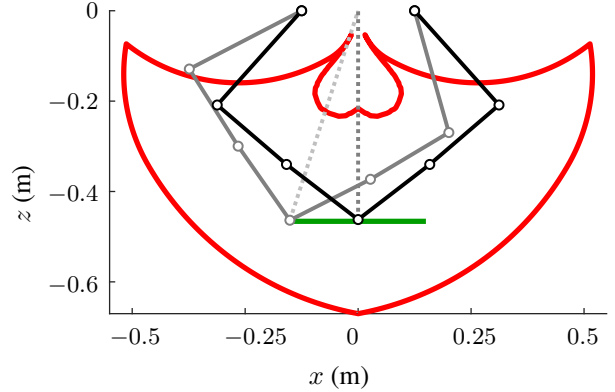
$$k_d = (1 + 2\xi)\omega \quad (23)$$

$$k_p = (1 + 2\xi)\omega^2 \quad (24)$$

$$k_i = \omega^3 \quad (25)$$



(a) Reference Trajectory for the robot end-effector.



(b) Reference trajectory for the robot end-effector (in green) given in the R-Min workspace with initial and median configuration obtained from the inverse geometrico-static model.

Fig. 7: Trajectory used for the evaluation of the controller performances.

where, for our prototype, the damping coefficient  $\xi$  is fixed at 0.72 and the controller cut-off pulsation  $\omega$  is experimentally set at 22 rad/s.

## 4.3 Experimental evaluation of the controller performances

In this section, the tracking performances of the controller are evaluated experimentally on the prototype of the R-Min robot. A reference trajectory is defined in the Cartesian space. It consists of a linear, horizontal trajectory of 30 cm generated using a quintic polynomial motion law so as to reach a maximal linear velocity of the end-effector of 1.5 m/s (see Fig. 7). From this trajectory, the desired motor positions, velocities and accelerations  $\mathbf{q}_a^*(t)$ ,  $\dot{\mathbf{q}}_a^*(t)$  and  $\ddot{\mathbf{q}}_a^*(t)$  (the controller inputs) are computed using the dynamic model. It should be noted that the dynamic model was previously validated experimentally by a proper comparison of simulation and experimental results, whose details are not shown in this article.

The tracking errors on motor coordinates were mea-

sured using the motor encoders. Results are presented in Fig. 8a, showing a maximal error of 3.2 deg. This value is relatively low regarding the simplicity of the used controller and seems low enough to achieve pick-and-place operations. The tracking error at the level of the end-effector was obtained from a camera<sup>3</sup>. Results are presented in Fig. 8b and show a maximal error of 17 mm along the x direction and 14 mm along the z direction. At the end of the motion, a residual error of 4 mm is probably due to the presence of dry friction into the passive joints and to encoder calibration errors which are not compensated. These errors appear to be reasonable for a pick-and-place application. Figure 8c shows the evolution of the passive angles  $q_{13}$  and  $q_{23}$  along the trajectory. A maximal amplitude of  $9.3^\circ$  is reached which indicates that the amplitude of these uncontrolled internal motions remains low enough not to represent an additional risk for human operators.

## 5 EXPERIMENTAL ANALYSIS OF THE SAFETY PERFORMANCES OF THE R-MIN ROBOT

In this section, we first introduce the experimental setup that will be used in order to analyze experimentally the safety performances of the R-Min robot and to compare them with those of the five-bar mechanism. Following the recommendations given in the standard ISO 15066 [20], the maximum impact force is chosen as the safety criteria. This impact force is measured using a dedicated Impact Force Measurement Device (IFMD), that will be presented below. This IFMD allows to mimic the bio-mechanical properties of different parts of the human body, in case of a constrained impact (i.e. when the human body is clamped between the robot and a wall or the ground). Multiple impact scenarios are conducted in order to evaluate the effects of different parameters on safety such as the configuration of the robot, the location of the impact on the robot (at the end-effector or on middle of the distal arm), the velocity of the end-effector at the time of impact, the impacted human body part or the stiffness of the preload spring.

### 5.1 Description of the experimental setup

#### 5.1.1 Description of the compared robots

The experimental setup is constituted of two robots: a prototype of R-Min presented in Sec. 2.2 and a five-bar mechanism. The five-bar mechanism is obtained by lock-

<sup>3</sup>A high-frequency camera is used to obtain, *a posteriori*, the joint and Cartesian coordinates of the robot. The camera used is a Mikrotrotron MC4082, images were acquired at a frequency of 500 Hz with a resolution of 1500 dpi. The camera is not used in the control of the robot.

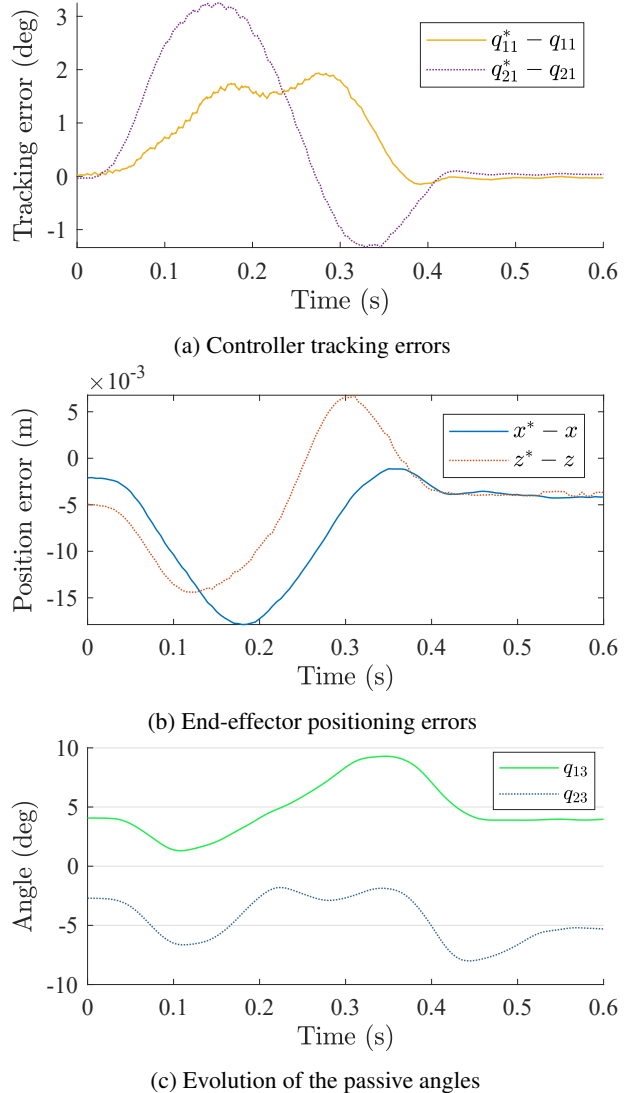


Fig. 8: Evolution of (a) the controller tracking errors, (b) the positioning error at the end-effector and (c) the passive angles  $q_{13}$  and  $q_{23}$  obtained during the reference trajectory with the R-Min robot ( $k_t = 111.2$  N/m).

ing the passive joints at  $O_{13}$  and  $O_{23}$  of the R-Min robot and by removing the preload bar. This permits to obtain two robots with comparable geometric and inertia properties. The R-Min robot is controlled using the strategy given in Sec. 4.2, whereas the five-bar mechanism is controlled using a standard Computed Torque Control [33]. Additionally, in the controller, an impact detection was settled to avoid the application of a continuous force on the impacted body after the collision. Once an impact is detected, the controller generates motor torques that compensate gravity effects only. As mentioned in the previ-

ous section, a high-frequency camera allows to measure the instant configuration of the robot and obtain its time-derivatives numerically.

### 5.1.2 Impact Force Measurement Device (IFMD)

The impact force is measured using a dedicated Impact Force Measurement Device (IFMD) which allows to mimic the bio-mechanical properties of different body parts such as the stiffness of the impacted body part and the non-linear properties of the skin, in case of a constrained impact. In accordance with the protocols given in [24, 23], this system is composed of a translating impactor, a changeable spring, a changeable soft material cover (foam) and a force sensor. The stiffness of the spring and the hardness and thickness of the foam are specified for 29 body parts in a document of the DGUV [25]. These protocols [24, 23] also recommend measuring the pressure during the collision, however, since the current paper focuses on the effect of the robot's architecture on safety and not on the local geometry of the robot where the contact occurs, the pressure was not measured. The clamping force, which is another important safety criteria [20] when considering a constrained impact, is not analyzed either in our evaluation. Indeed, thanks to the impact detection implemented in the controller and the subsequent reaction applied on motor torques, the clamping force is systematically null.

For the needs of the experiments, we designed our own IFMD (see Figs. 9a and 9b) following the recommendations given in [25, 24, 23]. It is constituted of the following parts:

- an impactor of mass  $m_p$  linked to the ground through a prismatic joint,
- a set of three foams with different Shore A hardness and thickness  $\ell_f$  (this set was provided by the Pilz company),
- a set of three springs with different stiffnesses  $k_h$ ,
- a force sensor Delta IP 68, with a measurement range of 1980 N along the impact direction, a resolution of 0.5 N, a data acquisition frequency of 7 kHz. The signal is filtered with a 4<sup>th</sup> order low-pass butterworth filter with a 3 dB frequency of 1 kHz,
- a stiff positioning table to position the force sensor with respect to the chassis of the robot.

The foam and the spring were chosen to match the properties of three different body parts: the belly, the leg and the head, as displayed on Tab. 3. These three body parts were selected because they represent the range of body stiffnesses given in the standards ISO/TS15066 [20] from 10 to 150 N/mm and use the three possible foams.

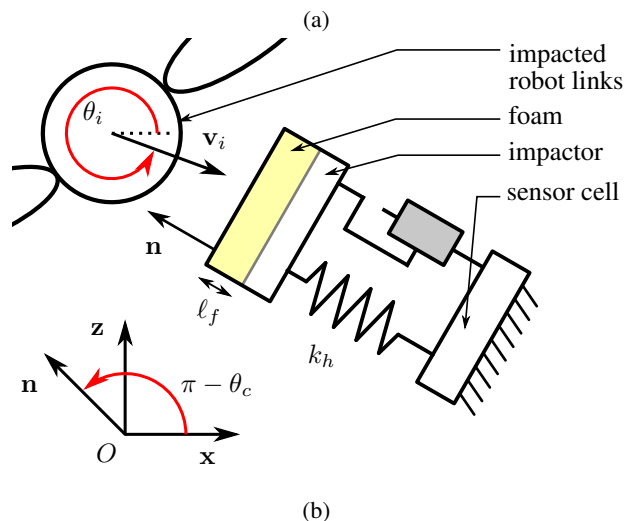
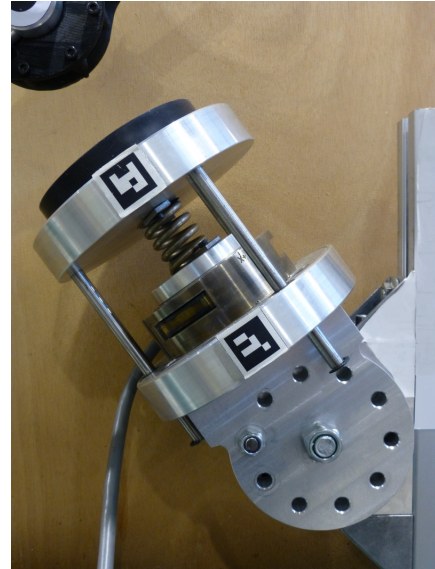


Fig. 9: Picture of the designed Impact Force Measurement Device (IFMD) mounted on the positioning table (a) and its schematic (b).

As shown in Tab. 3, the stiffnesses of the springs selected within the manufacturer's catalogue differ from the recommended values in [20] for multiple reasons related to the mechanical design. However, it is not our objective in this article to assess the safety of the R-Min robot, but only to compare its safety performances with respect to the five-bar mechanism.

## 5.2 Experimental protocol

In the following, we explain how we designed our experiment by detailing the impact scenarios that were

Table 3: Parameters of the IFMD used in the experiments,  $k_h$  is the stiffness given by the manufacturer, whereas  $k_h^{rec}$  is the stiffness recommended in the standard [20].

Body part	foam hardness	$l_f$	$m_p$	$k_h$	$k_h^{rec}$
	ShA	mm	kg	$\text{N}(\text{mm})^{-1}$	$\text{N}(\text{mm})^{-1}$
belly	10	21	1.72	11.3	10
upper leg	30	14	1.64	43	50
skull and forehead	70	7	1.57	116	150

selected for testing. We therefore introduce four reference impact configurations. From these impact configurations, multiple impact scenarios are defined in order to evaluate the effect of the following parameters on impact forces: the end-effector velocity, the impacted body part and the stiffness of the R-Min robot.

### 5.2.1 Definition of tested Impact Configurations (IC)

We introduce here four reference impact configurations defined by the configuration of the robot at the time of impact, the direction of the end-effector’s velocity and the location of the impact on the robot’s arm. These impact configurations are presented on Fig. 10 and can be summarized as follows:

- Configuration “Co” corresponds to an impact on the distal arm (in the middle of link (2, 2) for the five-bar mechanism, on  $O_{23}$  for R-Min), while the robot is in a centred configuration (Fig. 10a),
- Configuration “Cp” corresponds to an impact on the end-effector  $P$ , while the robot is in a centred configuration (Fig. 10b),
- Configuration “So” corresponds to an impact on the distal arm (in the middle of link (2, 2) for the five-bar mechanism, on  $O_{23}$  for R-Min), while the robot is in a side-configuration (Fig. 10c),
- Configuration “Sp” corresponds to an impact on the end-effector  $P$ , while the robot is in a side-configuration (Fig. 10d).

We did not consider any impact with the proximal arm (link ( $i$ , 1)), since we assume that a proper protective housing could be designed to avoid any contact with the proximal arm of the robot.

In the collision protocols furnished by the COVR consortium [24, 23], it is recommended to position the IFMD such that the foam surface is normal to the direction of the velocity of the contact point attached to the robot  $\mathbf{v}_i$ . However, this protocol is well-adapted for serial robots, when impact occurs on the end of the arm. In our case, due to the parallel architecture of the robot and

Table 4: Set of parameters defining the four reference Impact Configurations (IC). The orientation of the impact velocity  $\theta_i$  is computed from the quasi-static configuration and may vary slightly for the R-Min robot due to internal dynamics of passive joints.

IC	$x(t_c)$	$z(t_c)$	$\theta_e$	$\theta_c$	$\theta_i$
	$m$	$m$	deg	deg	deg
Co	0	-0.48	-37.5	-45	-38.3
Cp	0	-0.41	-30	-54	-30
So	0.15	-0.46	0	-36	-7.7
Sp	0.15	-0.48	0	-36	0

its bulky nature, the IFMD was positioned normal to the distal arm at the time of impact (see Fig. 10), so that the contact is punctual and takes place on the foam surface and not on its sides.

Table 4 regroups the main parameters defining each four impact configurations, i.e. the end-effector’s coordinates at the time of impact, the orientation of the end-effector’s velocity vector  $\theta_e$ , the orientation of the IFMD  $\theta_c$  and the orientation  $\theta_i$  of the velocity vector of the contact point. This latter angle is not measured but computed using the geometrico-static model given in Sec. 3.

### 5.2.2 Impact scenarios

The design of experiments is based on multiple impact scenarios defined by the selected impacting robot (R-Min, R-Min<sup>+</sup> or five-bar mechanism), the impacted body part (belly, leg or skull head) and the selected impact configuration (as defined in Tab 4 and Fig. 10). Impact scenarios have been selected in order to allow the comparison of the R-Min robot with the five-bar mechanism from a safety perspective and to evaluate the effect of the following parameters on impact forces: the configuration of the robot, the location of the impact on the robot’s arm, the impacted body part (belly, leg or head), the stiffness of the preload bar and the end-effector’s velocity. Therefore,

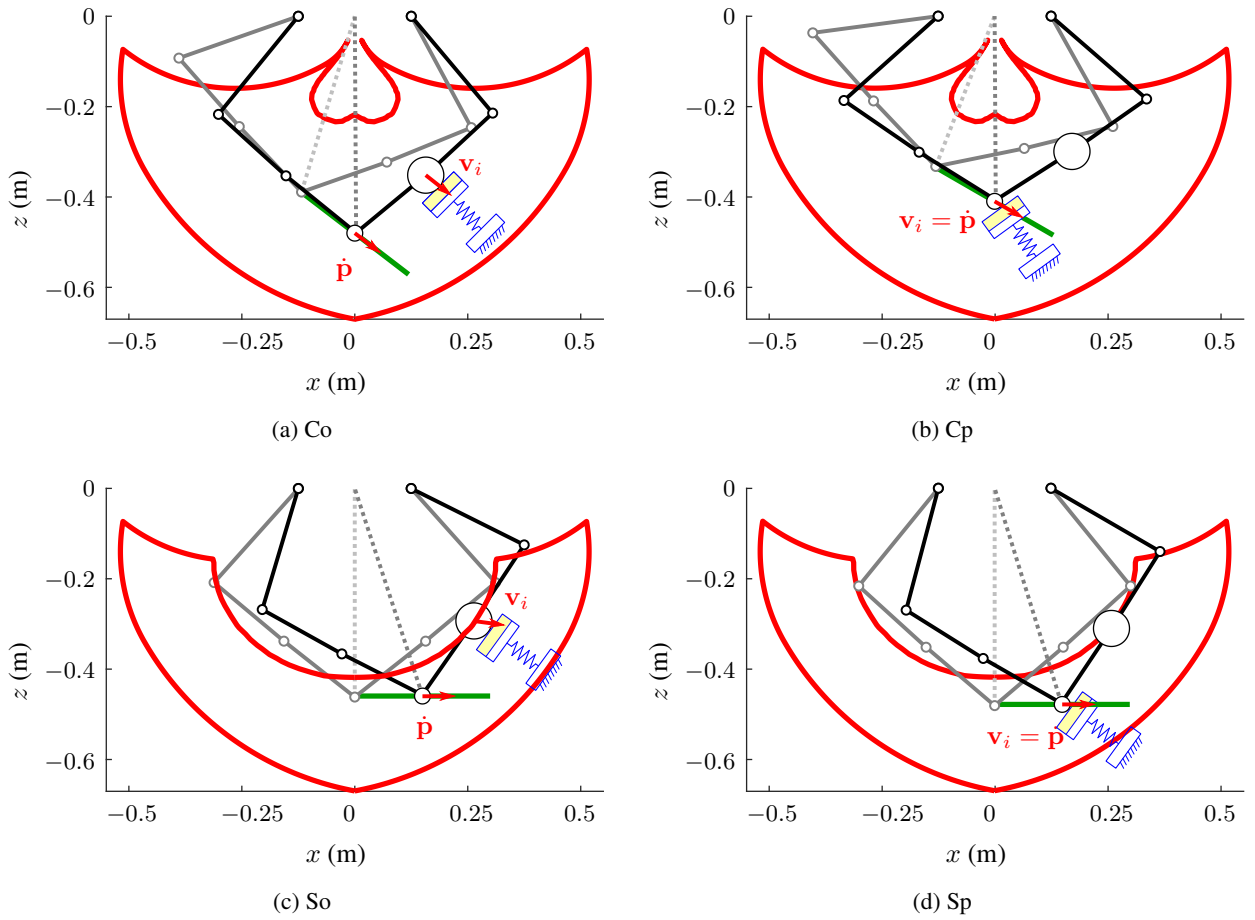


Fig. 10: Representation of the four reference impact configurations (a) Co, (b) So, (c) Cp and (d) Sp. The trajectory is represented in green, the robot is drawn in the initial configuration (grey) and at the time of impact (black). The workspace is drawn for two different cases: (a-b) R-Min and (c-d) R-Min+. The velocity of the end-effector and that of the impact point, as well as the location of the sensor are shown for each of the four reference impact configurations.

we propose the following design of experiments:

- Eight impact scenarios are defined to analyze the effect of the impact configuration on impact forces. Both robots (R-Min and the five-bar mechanism) are tested impacting the IFMD set to mimic the head. The four impact configurations are considered: Co, Cp, So, Sp.
- Eight additional impact scenarios are defined to analyze the effect of the impacted body part on impact forces. Both robots are tested impacting the IFMD in two additional settings (belly and leg). Two impact configurations are considered: Co, Cp.
- Two additional impact scenarios are defined to analyze the effect of the stiffness of the spring of the preload bar on impact forces. We therefore con-

sider the R-Min<sup>+</sup> version of the R-Min robot which uses a set of springs with a larger stiffness ( $k_t = 231.9$  N/m). This robot is thus tested impacting the IFMD in two additional settings (belly and leg). Two impact configurations are considered: So, Sp. Impact configurations Co and Cp could be not tested for R-Min<sup>+</sup>, because the corresponding robot configurations are not inside the workspace due to the motor torque limitations.

- The 18 previously defined impact scenarios are realized imposing three different end-effector's velocities at the time of impact  $v_e(t_c) = \{1, 1.5, 2\}$  m/s in order to analyze its effect on impact forces.

In order to ensure the repeatability of the obtained measures, each impact scenario was repeated 5 times for

a given end-effector’s velocity. Experimental results are obtained with a good reproducibility, indeed we computed the standard deviation of the maximal impact force for each impact scenario and obtained an average standard deviation of 1.7 % and a maximum one of 4.0 % among all impact scenarios.

### 5.3 Experimental results and analysis

In this section, we present the experimental results obtained from the previously presented design of experiments. The time profile of the impact force was acquired for each of the 18 impact scenarios and each of the three end-effector’s velocities. These results allow to analyze the effect of various parameters on safety as detailed in the following.

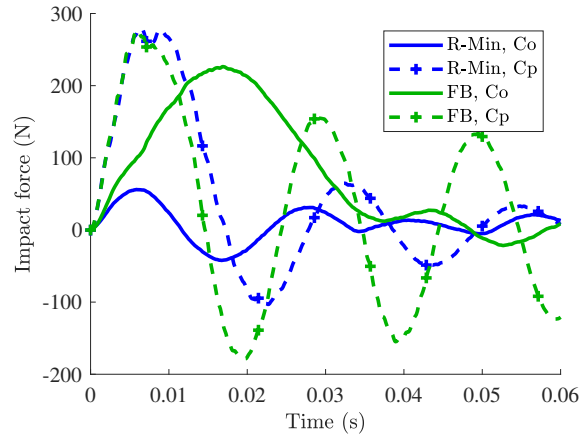
#### 5.3.1 Comparison of R-Min with the five-bar mechanism

In this section, we present the impact forces obtained using each of the two robots impacting with the IFMD set to mimic the head with an end-effector velocity  $v_e(t_c) = 1$  m/s. All four impact configurations are considered (Co, Cp, So, Sp).

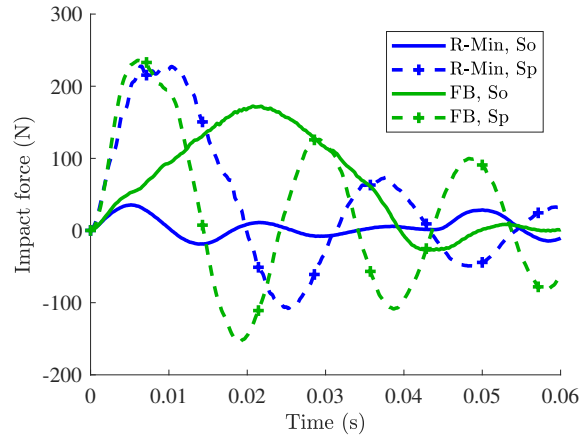
As can be seen on Fig. 11a, the maximum impact force obtained with the R-Min robot (56 N) is much lower than that obtained with the five-bar mechanism (226 N), when impact occurs on the distal arm with the robot being in a centred configuration (impact configuration Co). In this case, the maximum impact force is divided by a mean ratio<sup>4</sup> of  $r = 4.0$ . It should be noted that the impact duration is also significantly lower for the R-Min robot, showing that the mechanical energy transmitted to the human body part through the impact is much lower when using the R-Min robot.

However, when considering an impact at the level of the end-effector (Cp), the maximum impact forces are very similar for R-Min and the five-bar mechanism (280 N and 272 N respectively). In this case, the obtained mean ratio is  $r = 0.94$ . Similar results are obtained when considering the robot in a side-configuration (So, Sp) as depicted on Fig. 11b. We then obtain a mean ratio  $r = 4.6$  when impact occurs on the distal arm (So) and  $r = 1.01$  when impact occurs on the end-effector (Sp).

These results show that the underactuated architecture of the R-Min robot allows to significantly reduce the impact force when impact occurs on the middle of the distal arm at  $O_{23}$ , whereas the impact force can increase



(a) Impact config. Co and Cp



(b) Impact config. So and Sp

Fig. 11: Representation of the impact force time profile due to an impact between the R-Min robot or the five-bar mechanism and the head, with  $v_e(t_c) = 1$  m/s. The four impact configurations are considered: (a) Co and Cp, (b) So and Sp.

slightly when impact occurs on the end-effector. Indeed, as shown on Fig. 12a, the robot stiffness  $k_r$ <sup>5</sup> in the direction of impact of the R-Min robot is significantly lower than that of the five-bar mechanism, when considering an impact at point  $O_{23}$  for both centred and sided configurations. Interestingly, in this case, the stiffness of the R-Min robot is not isotropic but is particularly low in the direction of a probable impact (normal to the distal links 22 and 23), in contrast with the five-bar mechanism. Conversely, the R-Min stiffness is rather isotropic at the end-effector but larger than the stiffness of the five-bar mech-

<sup>4</sup>The ratio  $r$  is the division of the maximum impact force obtained with five-bar mechanism divided by the maximum impact force obtained with the R-Min robot. The ratio values given in this article correspond to the mean value obtained from five repetitions of an impact scenario.

<sup>5</sup>Appendix C details how the robot stiffness is computed.



anism (Fig. 12b).

This behaviour of the R-Min robot can be explained by the fact that, at the instant before collision, the distal links ( $i, 2$ ) and ( $i, 3$ ) are nearly aligned due to the tension applied in the preload bar, making the robot as stiff as the five-bar mechanism at the end-effector, independently of the stiffness of the preload bar. Figure 13b shows that the distal links of the R-Min robot remain aligned after an impact at the end-effector, in contrast with an impact at  $O_{23}$  as shown in Fig. 13a. For both robots, the stiffness at the end-effector mainly relies on the controller stiffness. Indeed, the stiffness of the robot mechanics at the end-effector is infinite when considering rigid links and joints, for both the five-bar mechanism and R-Min (considering aligned distal links in this latter case). The controller stiffness is given by the proportional gain  $k_p$  defined in Eq. (22), which depends on the inertia of the robot. This explains why the R-Min robot, whose inertia is larger than that of the five-bar mechanism, has a larger stiffness ellipsoid.

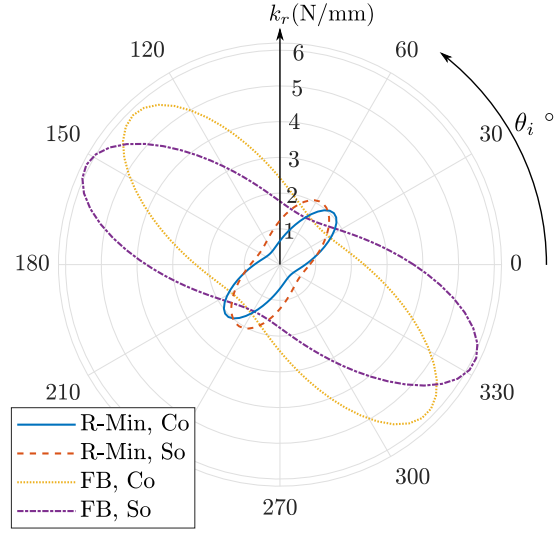
The introduction of a mechanical stop between links  $i2$  and  $i3$  on both arms, hindering the alignment of these two links, could help reducing the stiffness and the impact force at the end-effector, but, conversely, would increase the stiffness and the impact force at point  $O_{i3}$ . Authors believe a compromise could be found in the definition of this mechanical stop in order to obtain a safe behaviour at both locations, but did not investigate this idea in the present article.

In the following two sections, we check that these results remain true for different impacted body parts and different values of the end-effector velocity.

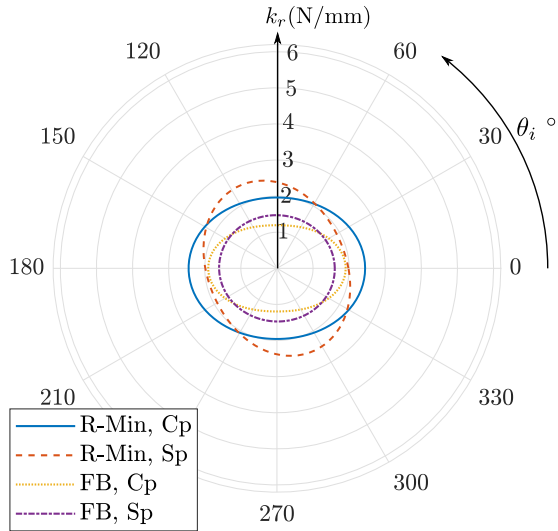
### 5.3.2 Effect of the impacted body on safety

We now investigate the effect of the impacted body part on the impact force. Therefore, three different settings of the IFMD are considered, in order to respectively mimic a constrained impact with the belly, the leg and the head (see Tab. 3). Both robots are considered in a centred configuration, impacting on distal arm (Co), with an end-effector velocity  $v_e(t_c) = 1$  m/s.

The corresponding impact force time profiles are presented on Fig. 14 and show that the maximum impact force is significantly lower for the R-Min robot than for the five-bar mechanism for each of the three body parts. A decreasing stiffness of the IFMD induces a decreasing value of the maximum impact force for both R-Min and the five-bar mechanism. A ratio  $r = 5.2$  is obtained for an impact on the belly,  $r = 4.2$  on the leg and  $r = 4.0$  on the head, showing that the R-Min has a very positive effect on safety in each of these three cases. Considering



(a) Robot stiffness at  $O_{23}$

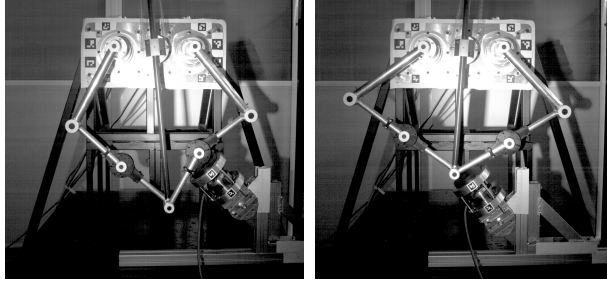


(b) Robot stiffness at the end-effector

Fig. 12: Representation of the robot stiffness ellipsoid of the R-Min robot and the five-bar mechanism, considering (a) an impact at the end-effector and (b) an impact at point  $O_{23}$ .

the impact configuration Cp, a ratio slightly lower than one is obtained in each case, as observed in the previous section.

To compare with, the admissible transient impact forces given in the standard ISO/TS 15066 [20] are, respectively, 260 N and 220 N for the leg and the belly. No value is given for the head since it is a critical zone with whom any contact must be avoided. Results depicted on Fig. 14 show that the R-Min allows to obtain a maximum



(a) Impact config. Co (b) Impact config. Cp

Fig. 13: Captures of the R-Min robot 100 ms after the collision, considering impact configurations (a) Co and (b) Cp, with  $v_e(t_c) = 1$  m/s.

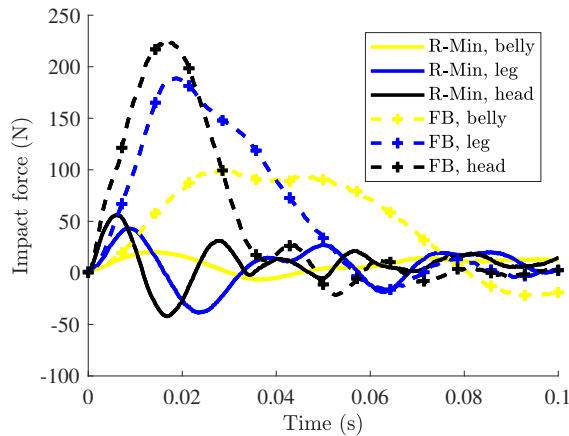


Fig. 14: Representation of the impact force time profile due to an impact between the R-Min robot (solid lines) or the five-bar mechanism (dashed lines), with different body parts (belly, leg and head). The impact configuration Co is considered with  $v_e(t_c) = 1$  m/s.

impact force that is significantly lower than the allowable thresholds for the leg and the belly and, thus, would allow operating at higher velocity, whereas the five-bar mechanism is already close to the maximum value, especially for the leg. However, this conclusion is not valid when impact occurs on the end-effector.

### 5.3.3 Effect of the end-effector velocity on safety

As mentioned in multiple works [14, 35], there exists a linear relationship between the maximum impact force and the velocity of the impact point at the time of impact  $v_i(t_c)$ . In what follows, we show that this linear relation is verified for each of the 18 impact scenarios.

Indeed, a linear regression going through the origin

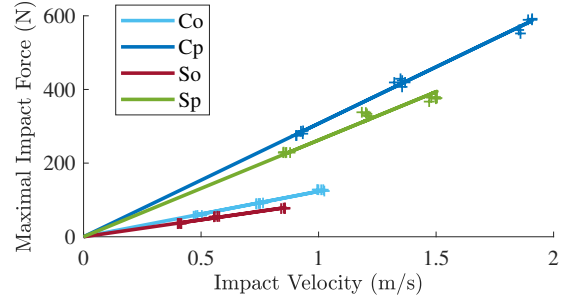


Fig. 15: Representation of the maximum impact force as a function of the velocity of the impact point considering the R-Min robot impacting with the head in all reference impact configurations. A linear regression is performed for each impact configuration and shows a linear behaviour of the impact force with respect to the velocity of the impact point.

was performed for each impact scenario, considering the three end-effector's velocities  $v_e(t_c) = \{1, 1.5, 2\}$  m/s (see Fig. 15). It is recalled that each impact scenario is led five times for each end-effector's velocity, providing 15 points for the linear regression. We obtain a maximum error on the maximum impact force of 12.0 % using the linear regression model, among all impact scenarios, with a mean standard deviation of 3.7 %. Once this linear relation has been determined for each scenario, it would be possible to determine, by extrapolation, the end-effector velocity, knowing the maximum admissible impact force defined in the ISO/TS 15066 standard [20].

### 5.3.4 Effect of the stiffness of the preload bar on safety

It was shown in Sec 3.2 that the stiffness of the preload bar influences the size of the workspace when considering motor torque limitations (Fig. 6). In this section, we analyze how it affects the safety performances of the R-Min robot. The impact force is measured for two different settings of the preload bar, for R-Min  $k_t = 111.2$  N/m and  $\ell_0 = 82.7$  mm (see Fig.6c) for R-Min<sup>+</sup>  $k_t = 239.2$  N/m,  $\ell_0 = 102.5$  mm (see Fig.6d).

Results are presented on Fig. 16 considering impact configurations So and Sp,  $v_e(t_c) = 1$  m/s and an impact with the head. These results show that the stiffness of the preload system has a very negligible effect on the impact force, whatever the location of the impact on the robot. When impact occurs on  $O_{i3}$ , a ratio  $r = 5.4$  (resp.  $r = 4.6$ ) is obtained with R-Min<sup>+</sup> (resp. R-Min), showing that the maximum impact force is even decreased when using a stiffer spring in the preload bar.

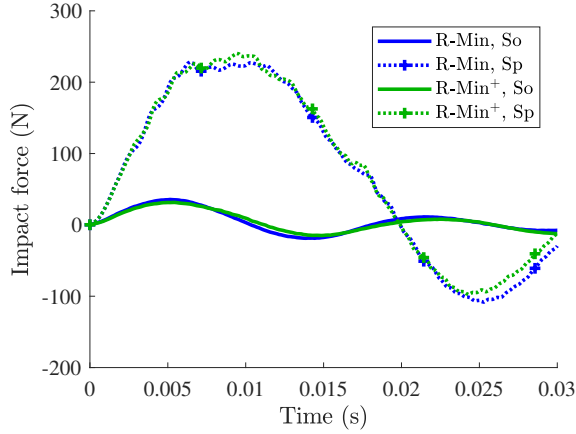


Fig. 16: Representation of the impact force time profile for two different stiffnesses of the preload bar: (a) R-Min and (b) R-Min<sup>+</sup>. Scenarios So and Sp are considered, with  $v_e(t_c) = 1$  m/s and an impact with the head.

## 6 CONCLUSION

This paper analyzed the safety performances of the R-Min robot, a planar underactuated parallel robot designed for intrinsically safe collaborations with human. After having introduced the mechanical architecture and presented its prototype, the workspace of the R-Min robot was computed numerically based on the geometrico-static, the kinemato-static models and a singularity analysis. The obtained workspace is very close to that of an equivalent five-bar mechanism. However, the R-Min workspace decreases as the stiffness of the spring in the preload bar increases due to practical motor torque limitations. The dynamic model of the R-Min robot was then introduced as well as the modified computed torque controller. An experimental analysis showed good tracking performances despite the underactuated nature of this robot.

In order to compare the safety performances of the R-Min robot with those of the five-bar mechanism, we set up a dedicated experimental setup, i.e. a five-bar mechanism with geometric and inertia properties equivalent to that of the R-Min robot, and a bio-fidelic Impact Force Measurement Device (IFMD). Following a detailed protocol, experimental results show that the underactuated architecture of the R-Min robot allows to reduce by a ratio of 4 to 5 the impact force with respect to the five-bar mechanism when impact occurs on the middle of the distal arm. In the meantime, when impact occurs on the end-effector, the impact force is similar to that obtained with the five-bar mechanism. The effect of the stiffness of the preload bar was shown to have a negligible effect on

the impact force. We also showed that there exists a linear relation between the impact force and the end-effector velocity for each scenario, allowing to determine, by extrapolation, the maximum end-effector velocity from the allowable impact force defined in the ISO 15066 standard.

The proof of concept R-Min allowed us to obtain encouraging results showing the interest of introducing underactuation in the mechanical architecture of a parallel robot to obtain an intrinsically safer robot. Therefore, further works will investigate strategies to reduce the impact force when impact occurs both on the distal arm or on the end-effector. We will also extend this planar architecture to the spatial case. Simulations tools will be used to optimize the design of such robot with respect to safety criteria. In parallel, we will investigate the use of flexible links in the mechanical design of a parallel robot to obtain a highly underactuated system.

## A EXPRESSION OF THE POTENTIAL ENERGY

The potential energy of the link  $(i, j)$  due to the gravity field, denoted as  $U_{i,j}$ , depends on the links masses  $m_{i,j}$  (respectively  $m_4$  and  $m_5$  for links (4) and (5)), their centre of mass position  $S_{i,j}$  (respectively  $S_4$  and  $S_5$ ) and their length  $\ell_{i,j}$ . The length  $\ell_{S_{i,j}}$  is equal to  $\ell_{O_{ij}S_{i,j}}$ .  $\ell_{S_4}$  is the length from  $P$  to  $S_4$ ,  $\ell_{S_5}$  is the length from  $A$  to  $S_5$ .

It is then possible to express the potential energy due to the gravity for each link:

$$U_{i,1} = gm_{i1}\ell_{S_{i1}} \sin(q_{i1}), \quad (26)$$

$$U_{i,2} = gm_{i2} (\ell_{i1} \sin(q_{i1}) + \ell_{S_{i2}} \sin(q_{i1} + q_{i2})) \quad (27)$$

$$U_{i,3} = gm_{i3} (\ell_{i1} \sin(q_{i1}) + \ell_{i2} \sin(q_{i1} + q_{i2}) + \ell_{S_{i3}} \sin(q_{i1} + q_{i2} + q_{i3})) \quad (28)$$

$$U_4 = gm_4 z (1 - \ell_{S_4}/\rho) \quad (29)$$

$$U_5 = gm_5 \ell_{S_5} \sin(q_4) = gm_5 \ell_{S_5} z / \rho \quad (30)$$

where the angle  $q_4 = \tan^{-1}(z/x)$  and the length  $\rho = \sqrt{x^2 + z^2}$  parameterize the configuration of the preload system.

The potential energy of the robot due to the gravity can then be summarized as:

$$U_\ell(\mathbf{q}_a, \mathbf{q}_d, \mathbf{p}) = \sum_{i=1}^2 \sum_{j=1}^3 U_{i,j}(\mathbf{q}_a, \mathbf{q}_d) + U_4(\mathbf{p}) + U_5(\mathbf{p}) \quad (31)$$

The potential energy of the spring included in the

preload system can be expressed as follows:

$$U_s = \frac{1}{2}k_t(\ell_4 - \rho - \ell_0)^2 \quad (32)$$

where  $k_t$  and  $\ell_0$  are respectively the stiffness and the free length of the spring and  $\ell_4$  is the length of the preload bar from the spring to the end-effector position.

As a result, the total potential energy of the robot  $U$  can be expressed as a function of the coordinates  $\mathbf{q}_a$ ,  $\mathbf{q}_d$  and  $\mathbf{p}$  by:

$$U(\mathbf{q}_a, \mathbf{q}_d, \mathbf{p}) = U_\ell(\mathbf{q}_a, \mathbf{q}_d, \mathbf{p}) + U_s(\mathbf{p}) - \mathbf{p}_c \mathbf{f} \quad (33)$$

where  $\mathbf{f}$  is an external force, assumed to be conservative, applied at a contact point  $\mathbf{p}_c$  of the robot.

## B EXPRESSION OF THE KINETIC ENERGY

The kinetic energy of the link  $(i, j)$  is denoted  $E_{i,j}$  and obtained as follows:

$$E_{i,1} = \frac{1}{2} (J_{i1} + m_{i1}\ell_{S_{i1}}^2) \dot{q}_{i1}^2 \quad (34)$$

$$E_{i,2} = \frac{1}{2} ((J_{i2} + m_{i2}\ell_{S_{i2}}^2) (\dot{q}_{i1} + \dot{q}_{i2})^2 + m_{i2}\ell_{i1}^2 \dot{q}_{i1}^2 + 2m_{i2}\ell_{i1}\ell_{S_{i2}}\dot{q}_{i1}(\dot{q}_{i1} + \dot{q}_{i2})\cos(q_{i2})) \quad (35)$$

$$E_{i,3} = \frac{1}{2} \left( (J_{i3} + m_{i3}\ell_{S_{i3}}^2) (\dot{q}_{i1} + \dot{q}_{i2} + \dot{q}_{i3})^2 + m_{i3}\ell_{i1}^2 \dot{q}_{i1}^2 + m_{i3}\ell_{i2}^2 (\dot{q}_{i1} + \dot{q}_{i2})^2 + 2m_{i3}(\ell_{i1}\ell_{i2}\dot{q}_{i1}(\dot{q}_{i1} + \dot{q}_{i2})\cos(q_{i2}) + \ell_{S_{i3}}(\dot{q}_{i1} + \dot{q}_{i2} + \dot{q}_{i3})(\ell_{i1}\dot{q}_{i1}\cos(q_{i2} + q_{i3}) + \ell_{i2}(\dot{q}_{i1} + \dot{q}_{i2})\cos(q_{i3}))) \right) \quad (36)$$

$$E_4 = \frac{1}{2} ((J_4 + m_4\ell_{S_4}^2) \dot{q}_4^2 + m_4\dot{x}^2 + m_4\dot{y}^2 - 2\ell_{S_4}\dot{q}_4(\cos(q_4)\dot{x} + \sin(q_4)\dot{y})) \quad (37)$$

$$E_5 = \frac{1}{2} (J_5 + m_5\ell_{S_5}^2) \dot{q}_5^2 \quad (38)$$

where  $J_{ij}$  ( $J_4$ ,  $J_5$ , resp.) is the moment of inertia around  $y$  of the body  $(i, j)$  (4, 5, resp.).

As a result, the total robot kinetic energy  $E$  can be expressed as a function of the coordinates  $\mathbf{q}_a$ ,  $\mathbf{q}_d$  and  $\mathbf{p}$ ,

and their time derivatives, by:

$$E(\mathbf{q}_a, \mathbf{q}_d, \mathbf{p}, \dot{\mathbf{q}}_a, \dot{\mathbf{q}}_d, \dot{\mathbf{p}}) = \sum_{i=1}^2 \sum_{j=1}^3 E_{i,j}(\mathbf{q}_a, \mathbf{q}_d, \dot{\mathbf{q}}_a, \dot{\mathbf{q}}_d) + E_4(\mathbf{p}, \dot{\mathbf{p}}) + E_5(\mathbf{p}, \dot{\mathbf{p}}) \quad (39)$$

## C EXPRESSION OF THE ROBOT STIFFNESS

Let us recall the static equilibrium equation presented on Eq. (4) :

$$\begin{cases} \nabla_{\mathbf{q}_{dp}} U(\mathbf{q}_a, \mathbf{q}_d, \mathbf{p}) + \nabla_{\mathbf{q}_{dp}} \boldsymbol{\phi}(\mathbf{q}_a, \mathbf{q}_d, \mathbf{p}) \boldsymbol{\lambda} = \boldsymbol{\tau}_e \\ \boldsymbol{\phi}(\mathbf{q}_a, \mathbf{q}_d, \mathbf{p}) = \mathbf{0} \end{cases} \quad (40)$$

where  $\boldsymbol{\tau}_e$  represents an external force applied on our mechanism, considered constant.

From equation (22), in static, we may consider that the controller acts like a spring system of stiffness matrix  $\mathbf{K}_p = (\mathbf{M}_{11} - \mathbf{M}_{12}\mathbf{M}_{22}^{-1}\mathbf{M}_{21})k_p$ , with a potential energy:  $U_a = 1/2(\mathbf{q}_a - \mathbf{q}_v)^T \mathbf{K}_p(\mathbf{q}_a - \mathbf{q}_v)$ ,  $\mathbf{q}_v$  being the motor desired reference. The equilibrium equation can be expressed using this additional spring:

$$\begin{cases} \left( \begin{array}{c} \nabla_{\mathbf{q}_{dp}} U(\mathbf{q}_a, \mathbf{q}_d, \mathbf{p}) \\ \nabla_{\mathbf{q}_a} U(\mathbf{q}_a, \mathbf{q}_d, \mathbf{p}) + \mathbf{K}_p(\mathbf{q}_a - \mathbf{q}_v) \end{array} \right) + \left( \begin{array}{c} \nabla_{\mathbf{q}_{dp}} \boldsymbol{\phi}(\mathbf{q}_a, \mathbf{q}_d, \mathbf{p}) \\ \nabla_{\mathbf{q}_a} \boldsymbol{\phi}(\mathbf{q}_a, \mathbf{q}_d, \mathbf{p}) \end{array} \right) \boldsymbol{\lambda} = \begin{pmatrix} \boldsymbol{\tau}_e \\ \mathbf{0} \end{pmatrix} \\ \boldsymbol{\phi}(\mathbf{q}_a, \mathbf{q}_d, \mathbf{p}) = \mathbf{0} \end{cases} \quad (41)$$

Differentiating Eq. (41), considering a small movement of the robot around this equilibrium configuration, due to an effort  $d\boldsymbol{\tau}$  applied on the mechanism, we obtain:

$$\begin{cases} \mathbf{H}d\mathbf{q}_t + \nabla_{\mathbf{q}_t} \boldsymbol{\phi} d\boldsymbol{\lambda} = d\boldsymbol{\tau} \\ \nabla_{\mathbf{q}_t} \boldsymbol{\phi}(\mathbf{q}_a, \mathbf{q}_d, \mathbf{p}) d\mathbf{q}_t = \mathbf{0} \end{cases} \quad (42)$$

with  $\mathbf{H}$  being the Hessian of the Lagrangian  $\mathcal{L} = U(\mathbf{q}_a, \mathbf{q}_d, \mathbf{p}) + U_a(\mathbf{q}_a, \mathbf{q}_v) + \boldsymbol{\phi}^T(\mathbf{q}_a, \mathbf{q}_d, \mathbf{p}) \boldsymbol{\lambda}$  with respect to variables  $\mathbf{q}_t = [\mathbf{q}_{dp} \ \mathbf{q}_a]^T$ .

The second part of Eq. (42) signifies  $d\mathbf{q}_t$  lies in the kernel of  $\nabla \boldsymbol{\phi}$ . Let us define  $\mathbf{Z} \in \mathbb{R}^{8 \times 2}$  a basis of the kernel of  $\nabla_{\mathbf{q}_t} \boldsymbol{\phi}^T$ ,  $d\mathbf{q}_t$  can be written under the form  $d\mathbf{q}_t = \mathbf{Z}\mathbf{v}$  with  $\mathbf{v} \in \mathbb{R}^2$ .

Left-multiplying the first line of Eq. (42) by  $\mathbf{Z}^T$  gives:

$$\mathbf{Z}^T \mathbf{H} \mathbf{Z} \mathbf{v} = \mathbf{Z}^T d\boldsymbol{\tau} \quad (43)$$

In the absence of Type 2 singularities, the projected Hessian  $\mathbf{H}_r = \mathbf{Z}^T \mathbf{H} \mathbf{Z}$  is invertible. Left-multiplying Eq. (43) by  $\mathbf{Z} \mathbf{H}_r^{-1}$  gives:

$$d\mathbf{q}_t = \mathbf{Z} \mathbf{H}_r^{-1} \mathbf{Z}^T d\boldsymbol{\tau} = \mathbf{S} d\boldsymbol{\tau} \quad (44)$$

with  $\mathbf{S}$ , being the softness matrix of the manipulator.

Considering a ponctual effort  $d\mathbf{f}_c$  applied at point  $\mathbf{p}_c$  applied on the mechanism, we have:

$$d\boldsymbol{\tau} = \mathbf{J}_c^T d\mathbf{f}_c \quad (45)$$

$$d\mathbf{p}_c = \mathbf{J}_c \mathbf{q}_t \quad (46)$$

with  $\mathbf{J}_c$  the contact Jacobian matrix.

We finally obtain:

$$d\mathbf{p}_c = \mathbf{J}_c \mathbf{S} \mathbf{J}_c^T d\mathbf{f}_c \quad (47)$$

where  $\mathbf{J}_c \mathbf{S} \mathbf{J}_c^T$  is the softness matrix at the point of contact and  $\mathbf{K}_c = (\mathbf{J}_c \mathbf{S} \mathbf{J}_c^T)^{-1}$ , the stiffness matrix. Projecting Eq. (47) along a direction  $\mathbf{n}$ , we obtain:

$$d\mathbf{p}_c = \mathbf{n}^T \mathbf{J}_c \mathbf{S} \mathbf{J}_c^T \mathbf{n} d\mathbf{f}_c = \frac{d\mathbf{f}_c}{k_r} \quad (48)$$

with  $k_r$ , the robot stiffness along direction  $\mathbf{n}$ .

## REFERENCES

- [1] Robla-Gómez, S., Becerra, V. M., Llata, J. R., Gonzalez-Sarabia, E., Torre-Ferrero, C., and Perez-Oria, J., 2017. “Working together: A review on safe human-robot collaboration in industrial environments”. *IEEE Access*, **5**, pp. 26754–26773.
- [2] Vicentini, F., 2021. “Collaborative Robotics: A Survey”. *Journal of Mechanical Design, Transactions of the ASME*, **143**(4), pp. 1–20.
- [3] Bischoff, R., Kurth, J., Schreiber, G., Koeppe, R., Albu-Schäffer, A., Beyer, A., Eiberger, O., Haddadin, S., Stemmer, A., Grunwald, G., and Hirzinger, G., 2010. “The kuka-dlr lightweight robot arm - a new reference platform for robotics research and manufacturing”. In *ISR 2010 (41st International Symposium on Robotics) and ROBOTIK 2010 (6th German Conference on Robotics)*, pp. 1–8.
- [4] Kim, Y.-J., 2017. “Anthropomorphic low-inertia high-stiffness manipulator for high-speed safe interaction”. *IEEE Transactions on robotics*, **33**(6), pp. 1358–1374.
- [5] Tsumaki, Y., Suzuki, Y., Sasaki, N., Obara, E., and Kanazawa, S., 2018. “A 7-dof wire-driven lightweight arm with wide wrist motion range”. In *2018 IEEE/RSJ International Conference on Intelligent Robots and Systems (IROS)*, pp. 1–9.
- [6] Pratt, G. A., and Williamson, M. M., 1995. “Series elastic actuators”. In *Proceedings 1995 IEEE/RSJ International Conference on Intelligent Robots and Systems. Human Robot Interaction and Cooperative Robots*, Vol. 1, pp. 399–406.
- [7] Bicchi, A., and Tonietti, G., 2004. “Fast and” soft-arm” tactics [robot arm design]”. *IEEE Robotics & Automation Magazine*, **11**(2), pp. 22–33.
- [8] Zinn, M., Roth, B., Khatib, O., and Salisbury, J. K., 2004. “A new actuation approach for human friendly robot design”. *The international journal of robotics research*, **23**(4-5), pp. 379–398.
- [9] Park, J.-J., Kim, B.-S., Song, J.-B., and Kim, H.-S., 2008. “Safe link mechanism based on nonlinear stiffness for collision safety”. *Mechanism and Machine Theory*, **43**(10), pp. 1332–1348.
- [10] Hyun, D., Yang, H. S., Park, J., and Shim, Y., 2010. “Variable stiffness mechanism for human-friendly robots”. *Mechanism and Machine Theory*, **45**(6), pp. 880–897.
- [11] López-Martínez, J., Blanco-Claraco, J. L., García-Vallejo, D., and Giménez-Fernández, A., 2015. “Design and analysis of a flexible linkage for robot safe operation in collaborative scenarios”. *Mechanism and Machine Theory*, **92**, pp. 1–16.
- [12] Zhang, M., Laliberté, T., and Gosselin, C., 2016. “On the design of mechanically safe robots based on spatial isotropic force modules and torque limiters”. *Mechanism and Machine Theory*, **105**, pp. 199–212.
- [13] Seriani, S., Gallina, P., Scalera, L., and Lughi, V., 2018. “Development of n-DoF Preloaded Structures for Impact Mitigation in Cobots”. *Journal of Mechanisms and Robotics*, **10**(5), 07. 051009.
- [14] Lauzier, N., and Gosselin, C., 2015. “A Comparison of the Effectiveness of Design Approaches for Human-Friendly Robots”. *Journal of Mechanical Design*, **137**(8), 08. 082302.
- [15] Campa, F., Diez, M., Diaz-Caneja, D., and Al-tuzarra, O., 2019. “A 2 dof continuum parallel robot for pick & place collaborative tasks”. In *IFTToMM World Congress on Mechanism and Machine Science*, Springer, pp. 1979–1988.
- [16] Jeanneau, G., Bégoc, V., Briot, S., and Goldsztejn, A., 2020. “R-min: a fast collaborative underactuated parallel robot for pick-and-place operations”. In *2020 IEEE International Conference on Robotics and Automation (ICRA)*, IEEE, pp. 10365–10371.

- [17] Versace, J., 1971. “A review of the severity index”. In Proc. 15th Stapp Car Crash Conf., SAE Technical Paper No. 710881, pp. 771–796.
- [18] Haddadin, S., Albu-Schäffer, A., and Hirzinger, G., 2007. “Safety evaluation of physical human-robot interaction via crash-testing”. In Robotics: Science and Systems, June 27-30, 2007, Georgia Institute of Technology, Atlanta, Georgia, USA, W. Burgard, O. Brock, and C. Stachniss, eds., Vol. 3, The MIT Press.
- [19] Haddadin, S., Albu-Schäffer, A., and Hirzinger, G., 2008. “The role of the robot mass and velocity in physical human-robot interaction-part i: Non-constrained blunt impacts”. In 2008 IEEE International Conference on Robotics and Automation, IEEE, pp. 1331–1338.
- [20] ISO/TC 299 : ISO/TS15066, 2016. Robots and robotic devices – Collaborative robots. Tech. Rep. ISO/TS15066, International Organization for Standardization, Tech. Rep, february.
- [21] Melia, M., Schmidt, M., Geissler, B., König, J., Krahn, U., Ottersbach, H. J., Letzel, S., and Muttray, A., 2015. “Measuring mechanical pain: the refinement and standardization of pressure pain threshold measurements”. *Behavior research methods*, **47**(1), pp. 216–227.
- [22] Yamada, Y., Hirasawa, Y., Huang, S., and Umetani, Y., 1996. “Fail-safe human/robot contact in the safety space”. In Proceedings 5th IEEE International Workshop on Robot and Human Communication. RO-MAN’96 TSUKUBA, pp. 59–64.
- [23] COVR, 2021. Test robot arm for collision with fixed object (measurement of pressure over time). Tech. Rep. ROB-LIE-2, COVR consortium.
- [24] COVR, 2021. Test robot arm for collision with a movable object (measurement of pressure over time). Tech. Rep. ROB-LIE-1, COVR consortium.
- [25] DGUV, 2017. Kollaborierende Roboter, Planung von Anlagen mit der Funktion ”Leistungs- und Kraftbegrenzung”. Tech. Rep. FB HM-080, DGUV.
- [26] Birglen, L., Laliberté, T., and Gosselin, C. M., 2007. *Underactuated robotic hands*, Vol. 40. Springer.
- [27] Jeanneau, G., Bégoc, V., and Briot, S., 2020. “Geometrico-static analysis of a new collaborative parallel robot for safe physical interaction”. In International Design Engineering Technical Conferences and Computers and Information in Engineering Conference, Vol. 10: 44th Mechanisms and Robotics Conference (MR). V010T10A067.
- [28] Quennouelle, C., and Gosselin, C., 2011. “Kinematostatic modeling of compliant parallel mechanisms”. *Meccanica*, **46**(1), jan, pp. 155–169.
- [29] Nocedal, J., and Wright, S., 2006. *Numerical optimization*. Springer Science & Business Media.
- [30] Black, C., Till, J., and Rucker, D., 2017. “Parallel continuum robots: Modeling, analysis, and actuation-based force sensing”. *IEEE Transactions on Robotics*, **34**(1), pp. 29–47.
- [31] Briot, S., and Goldsztejn, A., 2022. “Singularity conditions for continuum parallel robots”. *IEEE Transactions on Robotics*, **38**(1), pp. 507–525.
- [32] Merlet, J., 2006. “Jacobian, manipulability, condition number, and accuracy of parallel robots”. *ASME Journal of Mechanical Design*, **128**(1), pp. 199–206.
- [33] Khalil, W., and Dombre, E., 2002. “Chapter 14 - motion control”. In *Modeling, Identification and Control of Robots*, W. Khalil and E. Dombre, eds. Butterworth-Heinemann, Oxford, pp. 347–376.
- [34] Briot, S., and Khalil, W., 2015. *Dynamics of Parallel Robots: From Rigid Bodies to Flexible Elements*, 1 ed., Vol. 35 of *Mechanisms and Machine Science*. Springer International Publishing, Dordrecht, The Netherlands.
- [35] Herbster, S., Behrens, R., and Elkmann, N., 2021. “A new conversion method to evaluate the hazard potential of collaborative robots in free collisions”. In Experimental Robotics, B. Siciliano, C. Laschi, and O. Khatib, eds., Springer International Publishing, pp. 222–232.